Article

Immunity

Apolipoprotein E aggregation in microglia initiates Alzheimer's disease pathology by seeding β-amyloidosis

Graphical abstract

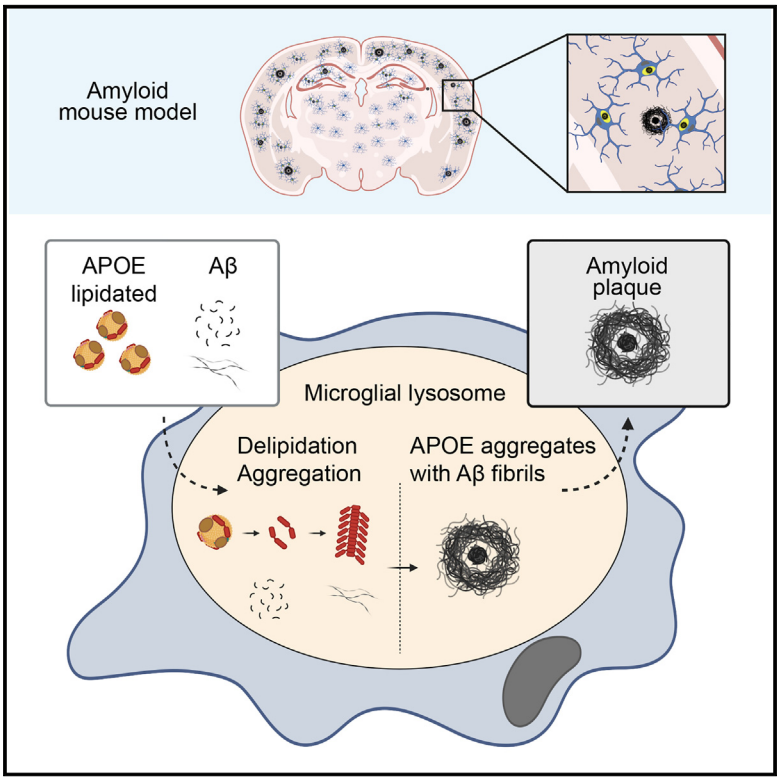

Authors

Seiji Kaji, Stefan A. Berghoff, Lena Spieth, ..., Oliver Wirths, Gesine Saher, Mikael Simons

Correspondence

stefan.berghoff@dzne.de (S.A.B.), mikael.simons@dzne.de (M.S.)

In brief

Pathogenic protein aggregation drives Alzheimer's disease, but how it is initiated remains unclear. By generating a APOE-HaloTag knockin mouse model and optimizing APOE purification techniques, Kaji et al. identify fibrillary APOE aggregates that can serve as seeds for Aβ plaque formation. This aggregation occurs within the endo-lysosomal system of microglia and is regulated by cholesterol metabolism.

Highlights

- Apolipoprotein E aggregates can serve as seeds for Aβ plaque pathology
- APOE aggregation occurs within the endo-lysosomal system of microglia
- APOE internalization is regulated by cholesterol metabolism in microglia
- Interferon-activated microglia facilitate the aggregation process

Kaji et al., 2024, Immunity *57*, 1–18
November 12, 2024
https://doi.org/10.1016/j.immuni.2024.09.014

CellPress

Immunity

CellPress
OPEN ACCESS

Article

Apolipoprotein E aggregation in microglia initiates Alzheimer's disease pathology by seeding β-amyloidosis

Seiji Kaji,[1,2,15] Stefan A. Berghoff,[1,2,15,*] Lena Spieth,[1,2,15] Lennart Schlaphoff,[1,2] Andrew O. Sasmita,[3] Simona Vitale,[1,2] Luca Büschgens,[4] Shreeya Kedia,[1,2] Martin Zirngibl,[1,2] Taisiia Nazarenko,[1,2] Alkmini Damkou,[1,2] Leon Hosang,[5] Constanze Depp,[3] Frits Kamp,[2,6] Patricia Scholz,[7] David Ewers,[3] Martin Giera,[8] Till Ischebeck,[7,9] Wolfgang Wurst,[2,10] Benedikt Wefers,[2,10] Martina Schifferer,[2,11] Michael Willem,[6] Klaus-Armin Nave,[3] Christian Haass,[2,6,11] Thomas Arzberger,[12,13] Sarah Jäkel,[14] Oliver Wirths,[4] Gesine Saher,[3] and Mikael Simons[1,2,11,14,16,*]

[1]Institute of Neuronal Cell Biology, Technical University Munich, Munich, Germany
[2]German Center for Neurodegenerative Diseases (DZNE), Munich, Germany
[3]Max Planck Insitute for Multidisciplinary Sciences, Göttingen, Germany
[4]Department of Psychiatry and Psychotherapy, University Medical Center (UMG), Georg-August-University, Göttingen, Germany
[5]Institute for Neuroimmunology and Multiple Sclerosis Research, Göttingen, Germany
[6]Metabolic Biochemistry, Biomedical Center (BMC), Faculty of Medicine, Ludwig-Maximilians University of Munich, Munich, Germany
[7]Department of Plant Biochemistry, University of Goettingen, Albrecht-von-Haller-Institute for Plant Sciences, University of Göttingen, Göttingen, Germany
[8]Leiden University Medical Center, Center for Proteomics and Metabolomics, Albinusdreef 2, 2333ZA Leiden, the Netherlands
[9]Institute of Plant Biology and Biotechnology (IBBP), Green Biotechnology, University of Münster, Münster, Germany
[10]Helmholtz Zentrum München, German Research Center for Environmental Health, Institute of Developmental Genetics, Neuherberg, Germany
[11]Munich Cluster of Systems Neurology (SyNergy), Munich, Germany
[12]Center for Neuropathology and Prion Research, Ludwig-Maximilians University of Munich, Munich, Germany
[13]Department of Psychiatry and Psychotherapy, Ludwig-Maximilians University Hospital, Munich, Germany
[14]Institute for Stroke and Dementia Research, University Hospital of Munich, LMU Munich, Munich, Germany
[15]These authors contributed equally
[16]Lead contact
*Correspondence: stefan.berghoff@dzne.de (S.A.B.), mikael.simons@dzne.de (M.S.)
https://doi.org/10.1016/j.immuni.2024.09.014

SUMMARY

The seeded growth of pathogenic protein aggregates underlies the pathogenesis of Alzheimer's disease (AD), but how this pathological cascade is initiated is not fully understood. Sporadic AD is linked genetically to apolipoprotein E (*APOE*) and other genes expressed in microglia related to immune, lipid, and endocytic functions. We generated a transgenic knockin mouse expressing HaloTag-tagged APOE and optimized experimental protocols for the biochemical purification of APOE, which enabled us to identify fibrillary aggregates of APOE in mice with amyloid-β (Aβ) amyloidosis and in human AD brain autopsies. These APOE aggregates that stained positive for β sheet-binding dyes triggered Aβ amyloidosis within the endo-lysosomal system of microglia, in a process influenced by microglial lipid metabolism and the JAK/STAT signaling pathway. Taking these observations together, we propose a model for the onset of Aβ amyloidosis in AD, suggesting that the endocytic uptake and aggregation of APOE by microglia can initiate Aβ plaque formation.

INTRODUCTION

Alzheimer's disease (AD) is preceded by a preclinical phase in which insoluble amyloid-β (Aβ) is deposited as extracellular plaques.[1] This gradual buildup of amyloid plaques is thought to trigger a pathological cascade involving multiple cell types, eventually leading to neurodegeneration with progressive deterioration of memory and cognitive function.[2,3] The seeded growth of self-replicating misfolded protein aggregates has served as a powerful conceptual framework in AD and other neurodegenerative diseases.[4–7] But what exactly initiates this pathological cascade? Genetic analyses have shown that the risk of sporadic AD is linked to genes that are primarily expressed in microglia and astrocytes, which respond to the deposition of amyloid protein,[8–16] but how these genes contribute to amyloidosis is not fully understood. The genetic determinants are found in immune, lipid, and endocytic pathways, and among the identified susceptibility genes, apolipoprotein E (*APOE*), with its allelic isoforms *APOE4*, confers the greatest risk.[11,17–19] Within the healthy central nervous system (CNS), APOE is mainly synthesized by

Please cite this article in press as: Kaji et al., Apolipoprotein E aggregation in microglia initiates Alzheimer's disease pathology by seeding β-amyloidosis, Immunity (2024), https://doi.org/10.1016/j.immuni.2024.09.014

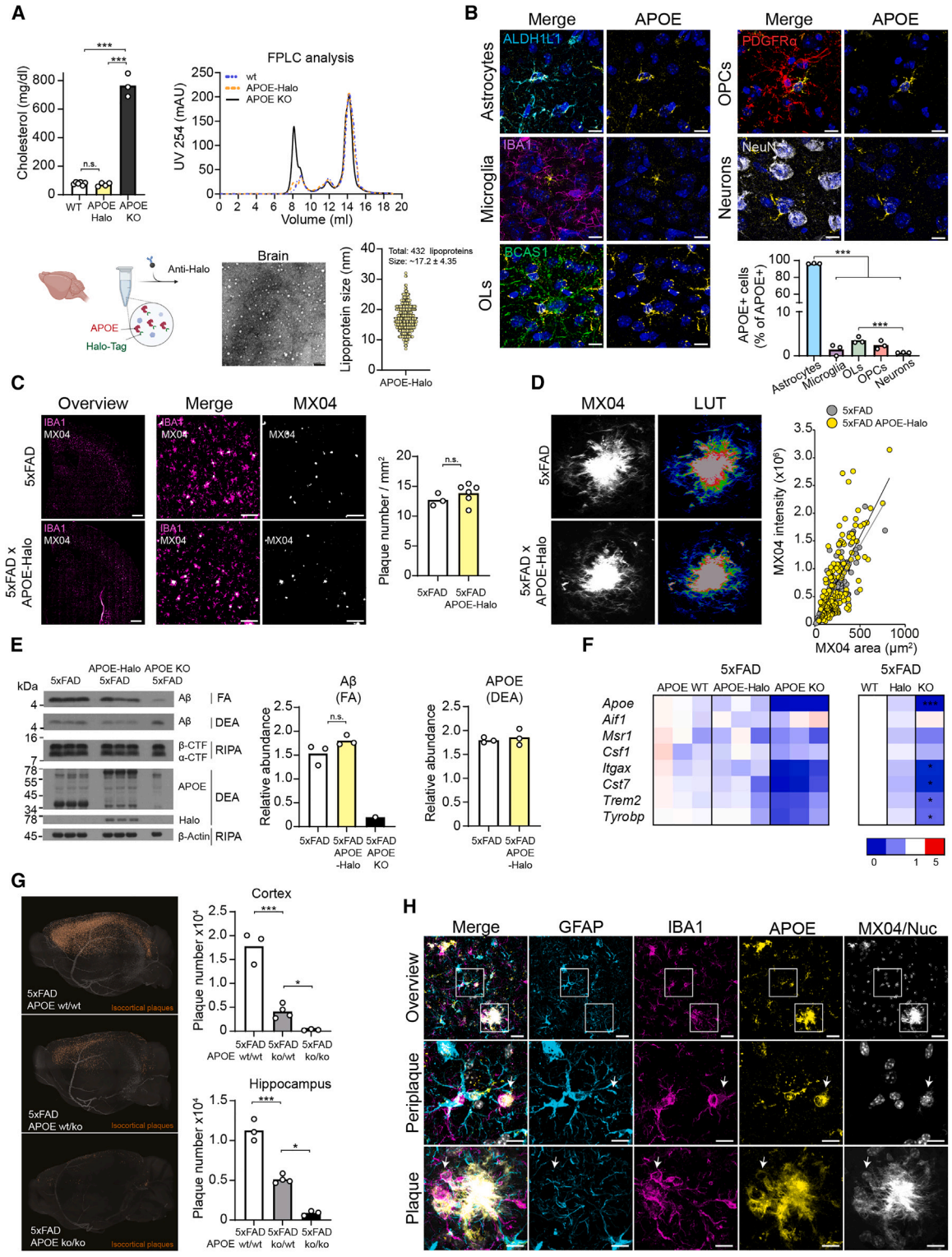

Figure 1. Generation and characterization of *ApoE-Halo* mice

(A) Cholesterol measurement and FPLC analysis of serum from 3-month-old *ApoE-Halo* and *ApoE KO* mice. Datapoints represent individual mice (n = 3–6). ***$p < 0.001$, one-way ANOVA with Tukey's post hoc test. FPLC was conducted by pooled serum from 4 to 5 female mice per group, and EM images show negative stain of lipoprotein particles immunopurified from *ApoE-Halo* mouse brain. Scale bar: 100 nm. Datapoints represent lipoparticles. See also Figures S1A–S1F.

(legend continued on next page)

Please cite this article in press as: Kaji et al., Apolipoprotein E aggregation in microglia initiates Alzheimer's disease pathology by seeding β-amyloidosis, Immunity (2024), https://doi.org/10.1016/j.immuni.2024.09.014

astrocytes, and similar to other apolipoproteins, APOE functions by solubilizing the lipids in the lipoprotein particle.[20–22] Through interaction with different members of the low-density lipoprotein family, the lipidated APOE particles are delivered by receptor-mediated endocytosis into cells, where the lipids support processes, such as cell viability, synaptogenesis, and membrane extension.[23–27] In addition to its physiological role in lipid homeostasis, APOE plays a key role in neurological diseases.[18,19,28] Virtually any injury to the CNS, including AD, results in microglia and astrocyte reactivity with an upregulation of lipid metabolic pathways and, in particular, APOE.[10,12,13,15] Studies in mice have shown that loss of APOE results in reduced fibrillary amyloid plaque deposition, indicating a role of APOE in Aβ fibrillization/stabilization and/or compaction.[29–31] Here, we developed a mouse model for optimized detection and purification of APOE, which enabled us to apply biochemical methods and to image APOE in a mouse model of Aβ amyloidosis with enhanced specificity. Using this experimental system, we identified fibrillary aggregates of APOE that facilitated Aβ amyloidosis within the lysosomal system of microglia, in a process modulated by immune and lipid metabolism.

RESULTS

Transgenic *ApoE-Halo* mice allow visualization and purification of APOE

To improve visualization and purification of APOE, we generated transgenic knockin mice expressing a HaloTag fused to mouse APOE (mAPOE) (*ApoE-Halo*). We found that cholesterol and cholesterol ester concentrations in the serum of homozygous *ApoE-Halo* mice were comparable to those of wild-type (WT) animals, unlike the elevated levels observed in APOE-deficient (*ApoE* knockout [*KO*]) mice (Figures 1A and S1A), verifying the physiologic functioning of carboxyl-terminal tagged APOE.[32] Next, we performed immunopurification experiments of Halo-tagged APOE from brain lysates and serum using Halo-Trap Magnetic Agarose. This method enabled the isolation of particles with the expected size of lipoproteins (17.2 nm ± 4.35 SD) as shown by electron microscopy (EM) (Figures 1A and S1B). Using real-time quantitative PCR, mass spectrometry-based analysis, and western blotting, we verified that the expression of genes involved in lipid metabolism, cholesterol ester abundance, and APOE protein abundance remained unaffected by the HaloTag within the brain (Figures S1C–S1E). Additionally, primary cultures of microglia demonstrated that the secretion of APOE-Halo was unchanged compared with WT APOE (Figure S1F). Next, we used fluorescent HaloTag ligand on brain sections of *ApoE-Halo* mice and validated astrocytes as the major APOE-expressing cell population in the adult cortex (Figures 1B, S1G, and S1H), with some expression in microglia and oligodendrocytes, as expected from previous studies.[33] To analyze APOE in experimental AD, we crossbred *ApoE-Halo* mice to the *5xFAD* model.[34] We determined plaque number and morphology by histologic labeling of fibrillar β sheet deposits using Methoxy-X04 (MX04), and the amount of soluble/insoluble Aβ by western blot analysis using diethylamine (DEA, soluble fraction) and formic acid (FA, insoluble fraction) as well as cleavage patterns of amyloid precursor protein (APP) by analyzing APP C-terminal fragments (CTFs) (Figures 1C–1E, S1I, and S1J). No differences in Aβ metabolism were detected between *5xFAD ApoE-Halo* compared with control mice (*5xFAD*). In addition, gene expression of APOE and microglial markers were not significantly altered in *5xFAD ApoE-Halo* mice (Figure 1F). These results were in contrast to *5xFAD* mice crossed with homozygous or heterozygous *ApoE KO* mice, which showed the expected gene dose-dependent reduction of Aβ deposits in histology (Figures 1G and S1K). Consistently, *5xFAD ApoE KO* revealed a strong reduction of insoluble Aβ and an increase of soluble Aβ (Figure 1E). Moreover, we used fluorescent HaloTag ligand to determine the cellular localization of APOE-Halo in *5xFAD* mice and detected an increase in microglia positive for APOE labeling in *5xFAD ApoE-Halo* mice (Figures 1B, 1H, and S1L). In addition, APOE-Halo was located to fibrillar β sheet-positive deposits (MX04$^+$) in cortical tissue samples (Figures 1H and S1M) and was recovered from the detergent-insoluble fraction of *5xFAD ApoE-Halo* mice brain lysates (Figure S1J). Thus, we have generated an *ApoE-Halo* knockin mouse for visualization and purification of APOE with no obvious alteration in lipid and Aβ metabolism.

APOE aggregates in *5xFAD* and human AD autopsies

The HaloTag self-labeling protein technology allowed us to determine APOE localization in Aβ plaques with high sensitivity and specificity. As expected,[35] we found that the majority of

(B) Fluorescent HaloTag ligand labeling for APOE visualization and immunostaining against cell-type markers. 3-month-old *ApoE-Halo* mice. Scale bar: 10 μm. Datapoints represent percentages of APOE$^+$ cells, ***$p < 0.001$, one-way ANOVA with Tukey's post hoc test. See also Figures S1G and S1H.

(C) Representative immunostaining of MX04$^+$ (gray) plaques and IBA1$^+$ (magenta) cells in *5xFAD* and *5xFAD ApoE-Halo* mice (6 months old, females) with corresponding quantification (middle). Scale bar: left, 500 μm and right, 100 μm. Datapoints represent individual mice ($n = 3–6$), **$p < 0.01$, Student's t test.

(D) Left: rainbow LUT to visualize intensity distribution of MX04 staining. Right: MXO4 intensity (IntDen) in relation to MX04$^+$ plaque size of *5xFAD* and *5xFAD ApoE-Halo* mice. Plaques are represented by single datapoints (>50 plaques per mouse, three female mice per group). See also Figure S1I.

(E) Immunoblot analysis of Aβ and APOE/Halo in formic acid (FA) and diethylamine (DEA)-extracted fractions, and analysis of C-terminal fragments of amyloid precursor protein in RIPA-extracted fractions from *5xFAD*, *5xFAD ApoE-Halo*, and *5xFAD ApoE KO* mice (6 months old, females). Quantifications show the relative abundance of Aβ (FA vs. DEA) and ApoE (DEA, normalized by β-actin). Datapoints represent individual mice ($n = 3$). One-way ANOVA with Tukey's post hoc test (Aβ) and Student's t test (APOE). See also Figure S1J.

(F) Quantitative PCR (qPCR) analysis of DAM signature genes and microglial markers of cortical samples from *5xFAD*, *5xFAD ApoE-Halo*, and 5xFAD *ApoE KO* mice (6 months old, females). Right: mean expression as fold-change to *5xFAD*, 3 mice per group, *$p < 0.05$, ***$p < 0.001$, one-way ANOVA with Tukey's post hoc test.

(G) 3D light-sheet microscopy analysis of plaques in *5xFAD ApoE*$^{+/+}$, *5xFAD ApoE*$^{+/-}$, and *5xFAD ApoE*$^{-/-}$ mice (4 months old, males). Representative images of Congo red (orange)-positive plaques in the isocortex with corresponding quantifications. Datapoints represent individual mice ($n = 3–4$), *$p < 0.05$, ***$p < 0.001$, one-way ANOVA with Tukey's post hoc test. See also Figure S1K.

(H) Representative immunostaining of APOE-Halo (yellow) in GFAP$^+$ (cyan) and IBA1$^+$ (magenta) cells and in MX04$^+$ (gray) plaques in periplaque/plaque area. White arrows indicate APOE-Halo$^+$ IBA1$^+$ cells. Scale bar: top, 200 μm and middle and bottom, 10 μm. See also Figures S1L and S1M.

Please cite this article in press as: Kaji et al., Apolipoprotein E aggregation in microglia initiates Alzheimer's disease pathology by seeding β-amyloidosis, Immunity (2024), https://doi.org/10.1016/j.immuni.2024.09.014

MX04$^+$ plaques were positive for Aβ and APOE labeling (APOE/Aβ intense plaques) at 3.5 months (82.1% ± 0.7% SEM) and 6 months of age (68.6% ± 6.0% SEM) in *5xFAD ApoE-Halo* mice (Figures 2A and S1M). With disease progression, we noted an increase in fibrillary Aβ plaques, which were positive for MX04 but with low labeling intensity for APOE (Aβ intense plaques) (increasing from 4.1% ± 0.4% SEM at 3.5 months to 19.7% ± 3.4% SEM at 6 months). Additionally, we found fibrillar MX04$^+$ deposits strongly positive for APOE-Halo ligand but with low amounts of Aβ (APOE-intense plaques). Quantification revealed that these MX04$^+$ structures occurred already early in the disease process and remained relatively stable over time with a proportion of 14% ± 1.0% SEM at 3 months of age and 11% ± 2.2% SEM at 6 months (Figures 2A and S2A). To rule out unspecific MX04 labeling, we used two additional β sheet-binding dyes, Thiazine red and Thioflavin, which confirmed the presence of APOE-intense β sheet-positive structures (Figure S2B). We extended these analyses to human AD autopsy samples and observed similar as in mice that the majority of MX04$^+$ plaques showed co-labeling of Aβ and APOE, with a subset displaying elevated amounts of either Aβ or APOE individually (Figure S2C).

To determine the relationship between APOE and Aβ aggregates *in vivo*, we developed a specific biochemical purification method based on the sarkosyl extraction optimized for Aβ fibril isolation[36] (Figure 2B). We took advantage of the detergent-insolubility of protein aggregates and prepared sarkosyl-insoluble *5xFAD ApoE-Halo* brain lysate fractions. As shown by western blotting, the use of 2% sarkosyl enabled the enrichment of both APOE and Aβ in sarkosyl-insoluble fractions compared with 1% sarkosyl (Figure S2D). Next, we applied the Halo-Trap Magnetic Agarose immune isolation system to purify APOE aggregates. We detected APOE-Halo but not Aβ in the immunopurified sarkosyl-insoluble faction, suggesting that some detergent-insoluble APOE aggregates exist almost independently of Aβ (Figures 2C and S2E). We performed native-PAGE and found that purified APOE-Halo aggregates from sarkosyl-insoluble fractions consisted as multimers (Figure S2F). EM revealed a wavy snake-like fibrillar morphology, consistent with previous reports from recombinant APOE,[37,38] which was positive for APOE immuno-gold labeling (Figures 2B and S2G). In addition, isolated APOE-Halo aggregates showed MX04 positivity after addition to microglial cell culture (Figure 2D). To determine whether APOE aggregates can also be purified from human AD brain autopsy samples, we established an aggregate purification protocol from AD cortex, which consists of 24 h incubation of brain lysates in 2% sarkosyl and immunopurification/immunodepletion by human APOE (hAPOE) and Aβ antibodies (Figures 2B and S2H). Since some hAPOE aggregates are tightly linked to Aβ fibrils, immunopurification of sarkosyl-insoluble APOE was followed by immunodepletion using Aβ antibodies, allowing isolation of APOE aggregates with higher purity (Figures 2C and S2I–S2K). We detected APOE but only minimal amounts of Aβ, and negative staining revealed wavy snake-like fibrillar morphology of the isolated aggregates obtained from both *APOE3/3* and *APOE4/4* AD autopsies, as observed in mice, which were positive for APOE immune-gold labeling (Figures 2B and S2G). Thus, APOE forms aggregates in *5xFAD* and human AD brains.

APOE aggregates act as a co-factor in Aβ pathology initiation

To determine whether the purified APOE aggregates can facilitate Aβ plaque formation, we conducted seeding experiments, which is an established tool to identify co-factors in plaque generation.[39,40] We made modifications to the previously reported protocols by conducting injections into the prefrontal cortex of *5xFAD* mice, wherein we applied the seeding material to one hemisphere and PBS to the other hemisphere, allowing us to obtain quantitative comparisons with a relatively low number of animals. The injections were administered at the onset of amyloid plaque formation (~8 weeks), and analysis was limited to 2 months post-injection to prevent potential cross-seeding into the opposite hemisphere. First, we established the experimental protocol using brain homogenates (PBS-extracted lysates) and sarkosyl-insoluble brain fractions from *5xFAD* mice. As shown previously,[41] both fractions led to enhanced seeding as determined by the ~2-fold increase in MX04$^+$ structures compared with the PBS injected hemisphere (Figure S3A). Having established the assay, we next determined the seeding activity of immunopurified APOE aggregates isolated from the sarkosyl-insoluble *5xFAD ApoE-Halo* brain fractions. Analysis of *5xFAD* mice injected with immunopurified mAPOE aggregates showed a significant elevation in number of MX04$^+$ structures (Figure 2E, left). MX04$^+$ signals colocalized with Aβ in a compacted morphology, indicating plaque generation (Figures 2E right and S3B). Seeding activity was diminished when APOE-Halo-depleted sarkosyl-insoluble fractions from 5xFAD mice were injected (Figure S3C). Additionally, when comparing seeding activity of sarkosyl-insoluble fractions from *5xFAD ApoE KO* mice to that from *5xFAD* mice (with Aβ content being adjusted to the same amount), fewer MX04$^+$ fibrillary aggregates were detected after injection of the APOE-deficient fractions (Figure S3D, right). Finally, we injected immunopurified APOE aggregates into *5xFAD ApoE KO* mice and detected MX04$^+$ APOE aggregates, which colocalized with Aβ (Figure S3E). Together, these experiments provide evidence for sarkosyl-insoluble APOE as a co-factor in Aβ plaque generation.

hAPOE aggregates act as a co-factor in Aβ plaque formation

To elucidate the impact of hAPOE on plaque formation, APOE3 and APOE4 knockin mice (*APOE3 KI*, *APOE4 KI*) were crossbred with *5xFAD* mice. First, we compared MX04$^+$ amyloid plaque number and detected a higher MX04$^+$ plaque load in *5xFAD APOE4 KI* compared with *5xFAD APOE3 KI* and *5xFAD* mice (Figures 3A, S4A, and S4B). Next, we asked whether brain-derived APOE aggregates from AD patients carrying either *APOE3/3* or *APOE4/4* (obtained by sarkosyl extraction and immunopurification from human AD autopsy samples, see Figure S2J) were able to act as a co-factor in Aβ plaque formation. We injected immunopurified APOE3 and APOE4 aggregates into *5xFAD* mice and found that both were able to enhance MX04$^+$ plaque formation as compared with control injections (Figures 3B and S4C). Subsequently, we injected the same immunopurified APOE aggregates from an AD patient into either *5xFAD APOE3 KI* or *5xFAD APOE4 KI* mice and observed that APOE aggregate injections increased amyloid plaque numbers compared with control injections in both mouse lines, with higher

Please cite this article in press as: Kaji et al., Apolipoprotein E aggregation in microglia initiates Alzheimer's disease pathology by seeding β-amyloidosis, Immunity (2024), https://doi.org/10.1016/j.immunu.2024.09.014

CellPress
OPEN ACCESS

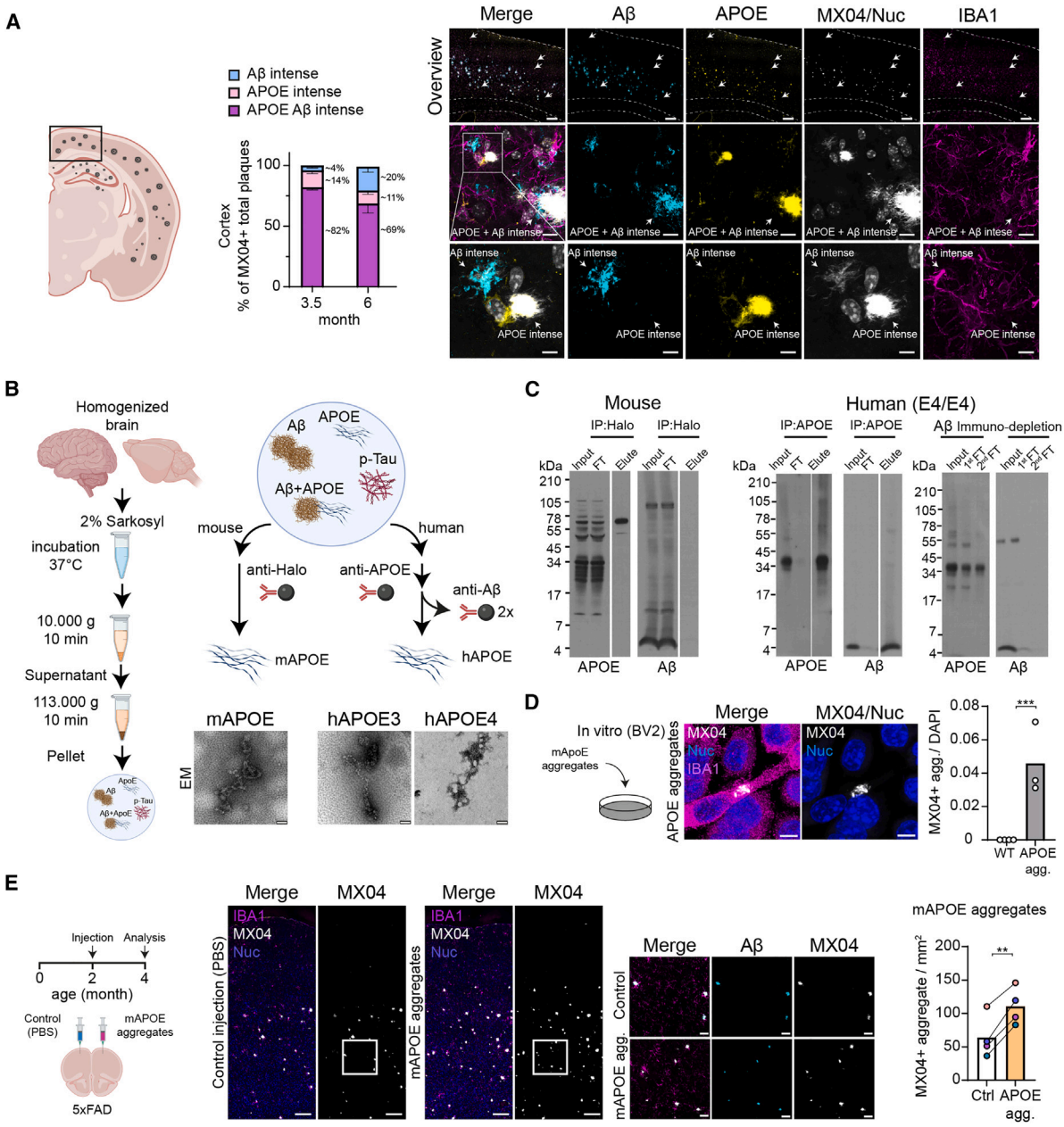

Figure 2. APOE forms aggregates in *5xFAD* and human AD autopsies

(A) Representative immunostaining of Aβ (cyan), APOE (yellow), and MX04 (gray) positive plaques in 6-month-old *5xFAD ApoE-Halo* male mice. White arrows in the overview indicate APOE-intense plaques. Scale bar: top, 200 μm; middle, 10 μm; bottom, 5 μm. Quantification of Aβ-intense, APOE-intense, and Aβ/APOE-intense plaques in 3.5- and 6-month-old *5xFAD ApoE-Halo* mice. Data are shown as mean percentage ± SEM (3 mice per group). See also Figures S2A–S2C.

(B) Schematic overview of mouse APOE (mAPOE) aggregate and human APOE (hAPOE) aggregate purification from *5xFAD ApoE-Halo* mice and sporadic AD patient material. Representative images show immunopurified aggregates by electron microscopy. Scale bar: 100 nm. See also Figures S2D, S2E, S2G, and S2H.

(C) Immunoblot analysis of purified mouse APOE aggregates (left) by Halo-immunoprecipitation and human APOE aggregates from AD brain (*APOE4/4*) (right) by APOE-immunoprecipitation combined with Aβ-immunodepletion. FT, flow-through. See also Figures S2F and S2I–S2K.

(D) Representative immunostaining shows MX04 (gray) positivity of immunopurified mouse APOE aggregates, which were internalized within IBA1$^+$ (magenta) BV2 cells. Scale bar: 5 μm. Datapoints represent individual cultures (n = 3–4), Student's t test, ***$p < 0.001$.

(E) Injection of immunopurified mouse APOE aggregates into the prefrontal cortex of 2-month-old female *5xFAD* mice. Tile scan images show the injection area with MX04 (gray), IBA1 (magenta), and Hoechst (Nuc, blue) staining 2 months post-injection. Scale bar: 100 μm. Magnified images showing the injected areas indicated by white rectangles with MX04 (gray), Aβ (cyan), and IBA1 (magenta) staining. Scale bar: 25 μm. Right: quantification of MX04$^+$ aggregates in injected areas. Datapoints represent individual mice (n = 4), **$p < 0.01$, Student's t test, lines connecting the datapoints indicate the comparison to PBS-control-injected contralateral site. See also Figures S3A–S3E.

Please cite this article in press as: Kaji et al., Apolipoprotein E aggregation in microglia initiates Alzheimer's disease pathology by seeding β-amyloidosis, Immunity (2024), https://doi.org/10.1016/j.immuni.2024.09.014

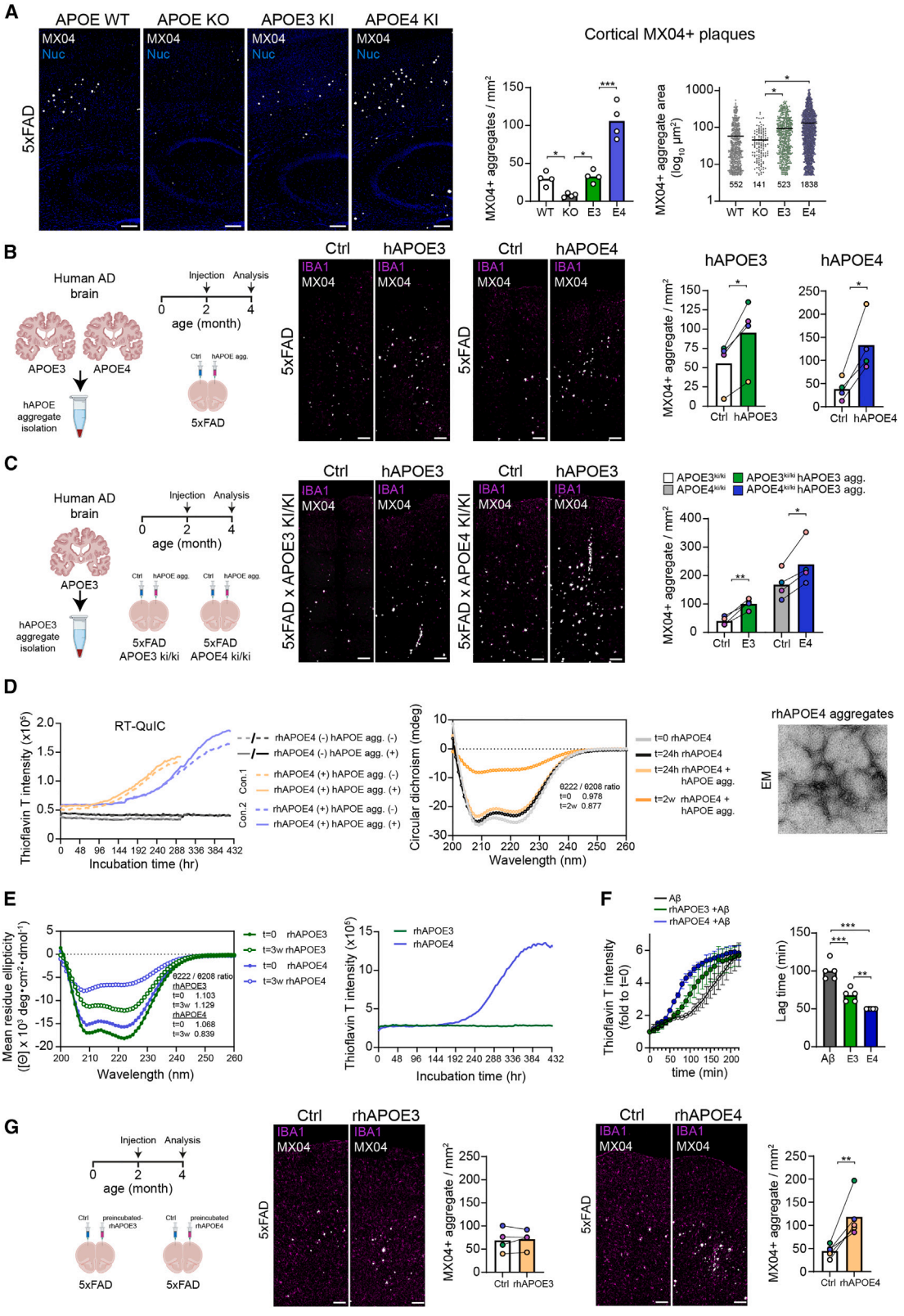

(legend on next page)

Please cite this article in press as: Kaji et al., Apolipoprotein E aggregation in microglia initiates Alzheimer's disease pathology by seeding β-amyloidosis, Immunity (2024), https://doi.org/10.1016/j.immuni.2024.09.014

MX04$^+$ plaque counts observed in *5xFAD APOE4 KI* mice (Figure 3C). Together, these experiments show that both APOE3 and APOE4 can act as a co-factor in Aβ plaque formation. To determine potential differences between the two APOE isoforms, we investigated their ability to aggregate *in vitro* and to function as seeds *in vivo*. We purified monomeric/tetrameric species of recombinant APOE3 and APOE4 via fast protein liquid chromatography (FPLC) and analyzed conformational changes over the incubation at 37°C for up to 4 weeks (Figures S4D–S4F). FPLC analysis detected the emergence of APOE4 in the higher molecular weight fractions, indicating aggregate formation (Figure S4F). To analyze how APOE4 changes its conformation, we performed real-time quaking-induced conversion (RT-QuIC) analysis. Analysis revealed increasing Thioflavin T fluorescence intensity of APOE4, which reached a plateau after 2 weeks (Figure 3D). In addition, abundance of α-helical structures and Θ222/Θ208 ratio were examined by circular dichroism (CD) spectroscopy, which showed markedly reduced α-helicity and loss of paired-coil structures post-incubation (Figure 3D). Finally, ultrastructural analysis of APOE4 aggregates after 2 weeks of incubation showed clusters of wavy fibrillar structures resembling *in vivo* isolated APOE4 aggregates (Figures 2B and 3D). When APOE3 was analyzed similarly, we did not observe altered Θ222/Θ208 ratio, increase in Thioflavin T fluorescence intensity, or drastic changes in molecular weight determined by FPLC (Figures 3E and S4G). Notably, when the assay was performed with APOE3 and APOE4 prepared as lipidated particles, no aggregation was detected indicating that lipidation hampers aggregation in cell-free environment (Figures S4G and S4H). Next, we performed a different type of RT-QuIC analysis using monomeric Aβ, which resulted in rapid increase in Thioflavin T fluorescence intensity compared with APOE. Co-incubating Aβ with 3-week preincubated recombinant hAPOE accelerated Aβ aggregation with APOE4 having a stronger effect on Aβ aggregation compared with APOE3 (Figure 3F). To determine whether *in vitro*-generated recombinant APOE4 aggregates can serve as a co-factor in amyloid plaque formation *in vivo*, we injected recombinant APOE4 aggregates into *5xFAD* mice and quantified MX04$^+$ plaque number (Figures 3G, S4I, and S4J). We detected a significant increase of MX04$^+$ amyloid plaques, which were co-labeled with antibodies against Aβ (Figure S4J). Injection of recombinant APOE3, prepared via a 3-week preincubation, did not result in an increase in the number of MX04$^+$ amyloid plaques in the seeding experiment (Figure 3G). Together, these findings show that *in vitro*-derived hAPOE aggregates can act as a co-factor in Aβ plaque formation similarly to *in vivo*-purified aggregates.

APOE-dependent Aβ seeding requires microglia

To understand how APOE promotes Aβ plaque formation, we determined the localization of APOE-Halo$^+$MX04$^+$ aggregates in *5xFAD ApoE-Halo* mice using confocal Airyscan detector for improved resolution. By applying 3D rendering, we noted labeling of APOE-Halo ligand and MX04 within IBA1$^+$ cells (Figures 4A and 4B). 3D image reconstruction revealed APOE-Halo$^+$MX04$^+$ profiles with small punctate staining or with larger fibrillary appearance within IBA1$^+$ cells, distinguishing these structures from extracellular plaques that typically associate with microglial cells (Figure S5A). APOE-Halo$^+$MX04$^+$ structures inside of IBA1$^+$ cells were often associated with CD68, a marker for

Figure 3. Human APOE aggregates induce Aβ pathology in *5xFAD*

(A) Tile scan images show cortex and hippocampus of 3-month-old female *5xFAD*, *5xFAD ApoE KO*, *5xFAD APOE3 KI*, and *5xFAD APOE4 KI* mice with MX04 (gray) and DRAQ5 (Nuc, blue) staining. Scale bar: 50 μm. Right: quantification of MX04$^+$ aggregates and violin plot showing the numbers and size distribution of MX04$^+$ aggregates. Datapoints represent individual mice (n = 4), $^*p < 0.05$, $^{***}p < 0.001$, one-way ANOVA with Tukey's post hoc test. See also Figures S4A and S4B.

(B) Injection of immunopurified APOE aggregates from human AD brains (*APOE3/3* and *APOE4/4* patient-derived) into the prefrontal cortex of 2-month-old male *5xFAD* mice. Tile scan images show the injection areas with MX04 (gray) and IBA1 (magenta) staining 2 months post-injection. Scale bar: 100 μm. Right: quantification of MX04$^+$ aggregates in injected areas. Datapoints represent individual mice (n = 4), $^*p < 0.05$, Student's t test, lines connecting the datapoints indicate the comparison to PBS-control-injected contralateral site. See also Figure S4C.

(C) Injection of immunopurified APOE aggregates from human AD brain (*APOE3/3* patient-derived) into the prefrontal cortex of 2-month-old female *APOE3 KI 5xFAD* and *APOE4 KI 5xFAD* mice. Tile scan images show the injection areas with MX04 (gray) and IBA1 (magenta) staining 2 months post-injection. Scale bar: 100 μm. Right: quantification of MX04$^+$ aggregates in injected areas. Datapoints represent individual mice (n = 4), $^*p < 0.05$, $^{**}p < 0.01$, Student's t test, lines connecting the datapoints indicate the comparison to PBS-control-injected contralateral site.

(D) Left: chronological amplification of β sheet structure in different preparations of recombinant human APOE (rhAPOE) by RT-QuIC analysis. Orange filled and dotted line: rhAPOE (0.5 mg/mL) + 10 μM Thioflavin T (100 μL of total volume) with/without human APOE aggregate from AD patient (*APOE3/3*) material, respectively. Blue filled and dotted line: rhAPOE (0.22 mg/mL) + 10 μM Thioflavin T (240 μL of total volume) with/without human APOE aggregate from AD patient material, respectively. Gray and black lines represent control buffer + 10 μM Thioflavin T in 100 and 240 μL of total volume, respectively (dotted line: without hAPOE aggregates, filled line with hAPOE aggregates). Middle: circular dichroism (CD) measurement before and after incubation (24 h and 2 weeks) of monomeric/tetrameric rhAPOE4 (0.15 mg/mL) in the presence or absence of isolated human APOE aggregates. Each value represents the average of 4 repeated measurements. Right: representative EM image shows the morphology of rhAPOE after 2-week incubation at 37°C. Scale bar: 100 nm. See also Figures S4D and S4E.

(E) Left: mean residue ellipticity measured by CD spectrometry before and after incubation (3 weeks) of monomeric/tetrameric rhAPOE3 and rhAPOE4. Right: chronological amplification of β sheet structure in rhAPOE3 and rhAPOE4 by RT-QuIC analysis. See also Figures S4F–S4H.

(F) Chronological amplification of β sheet structure in different preparations of monomeric Aβ-42 by RT-QuIC analysis. HFIP-treated Aβ-42 (10 μM) was incubated either with 3-week-preincubated rhAPOE3 or 3-week-preincubated rhAPOE4 (1 μg each). Equal amount of TBS was used as control. Datapoints represent mean values ± SEM of 5 analysis. Bar graph shows mean rag time of each sample to reach 2-fold increase from baseline, $^{**}p < 0.01$, $^{***}p < 0.001$, one-way ANOVA with Tukey's post hoc test.

(G) Injection of 3-week-preincubated rhAPOE3 and 3-week-preincubated rhAPOE4 (rhAPOE4 aggregates) into the prefrontal cortex of 2-month-old female *5xFAD*. Tile scan images show the injection area with MX04 (gray) and IBA1 (magenta) staining 2 months post-injection with the corresponding quantification of MX04$^+$ aggregates in injected areas on the right. Scale bar: 100 μm. Datapoints represent individual mice (n = 4), $^{**}p < 0.01$, Student's t test, lines connecting the datapoints indicate the comparison to PBS-control-injected contralateral site. See also Figures S4I and S4J.

Please cite this article in press as: Kaji et al., Apolipoprotein E aggregation in microglia initiates Alzheimer's disease pathology by seeding β-amyloidosis, Immunity (2024), https://doi.org/10.1016/j.immuni.2024.09.014

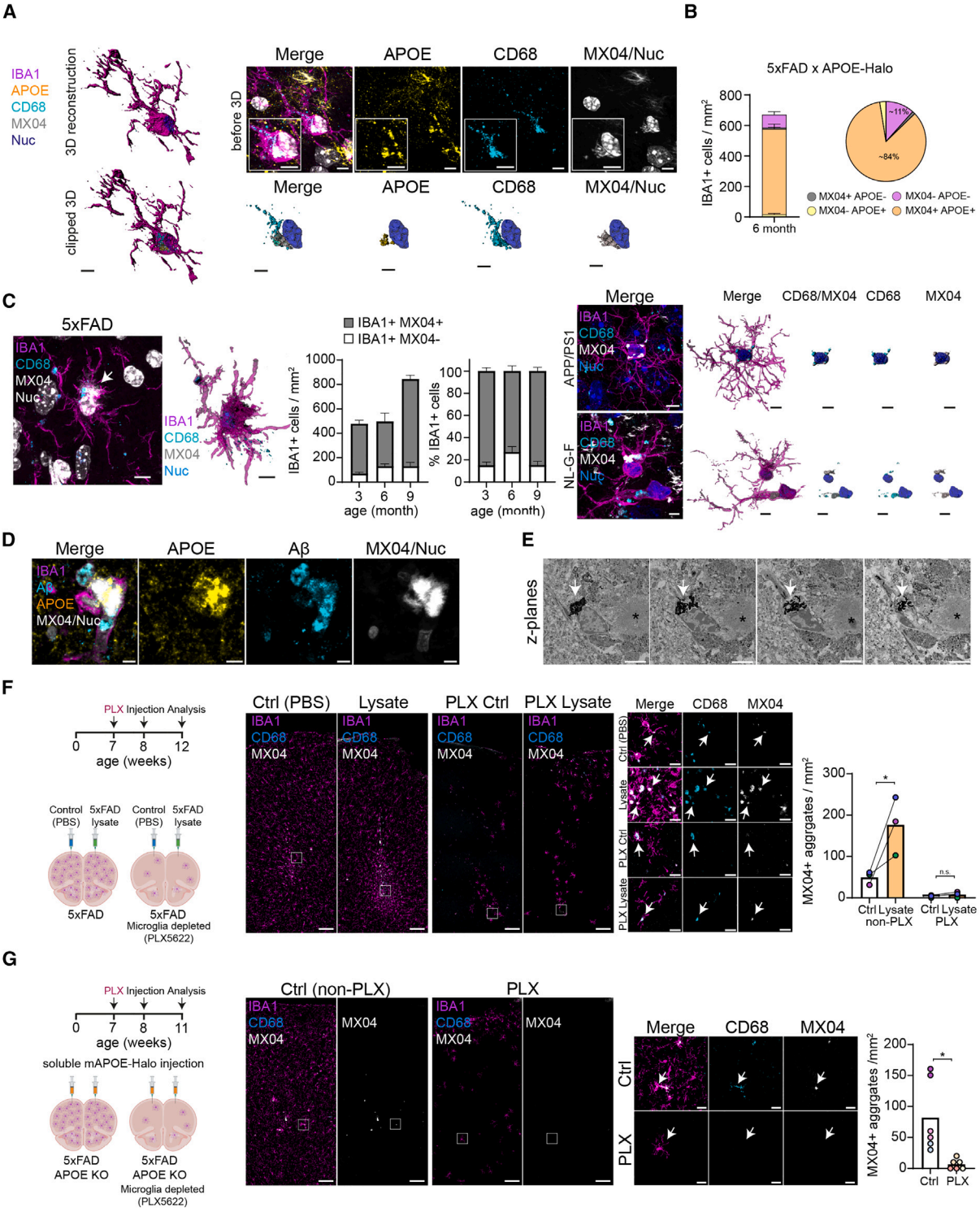

Figure 4. APOE-dependent Aβ seeding requires microglia

(A) Representative images (scale bar: 5 μm) and 3D reconstruction (scale bar: 2.5 μm) of APOE-Halo^{+} (yellow) MX04^{+} (gray) aggregates within IBA1^{+} (magenta) microglia of 6-month-old male *5xFAD ApoE-Halo* mice. Intracellular localization of aggregates is shown with nuclear (Hoechst, blue) and CD68^{+} (cyan) labeling. See also Figure S5A.

(B) Quantification of MX04^{+} aggregates colocalizing with APOE-Halo in 6-month-old male *5xFAD ApoE-Halo* mice. Bar graph data represent mean numbers of IBA1^{+} cells ± SEM (3 mice analyzed). Pie chart shows the mean percentages of MX04$^{+/-}$ APOE-Halo$^{+/-}$ cells among total IBA1^{+} cells.

(legend continued on next page)

endosomal/lysosomal compartment of activated microglia (Figures 4A, 4C, S5A, and S5B). Intracellular MX04$^+$ aggregates within microglia were not specific to the *5xFAD* AD model, as we detected these in two additional mouse models of AD (*APP/PS1* and *NL-G-F* mice) (Figure 4C), as well as in human autopsy samples (Figures 4D and S5C). By volume scanning EM, lysosomal aggregates in fibrillary morphology within microglial cells were detected, particularly in the periplaque area of *5xFAD ApoE-Halo* mice (Figures 4E and S5D). One possibility is that MX04$^+$APOE$^+$ aggregates form outside of microglia and are subsequently internalized for degradation. Alternatively, MX04$^+$ aggregates may develop inside microglia and then become released. To explore these possibilities, we pharmacologically depleted microglia using Plexxicon (PLX5622). First, we performed seeding experiment by injecting *5xFAD* brain lysates (PBS-extracted) into *5xFAD* mice that had been treated with either PLX5622 or normal control chow and found that MX04$^+$ aggregate formation was suppressed in PLX5622-treated mice as compared with the control-treated *5xFAD* mice (Figure 4F). Next, we conducted seeding experiments by injecting immunopurified RIPA-soluble APOE-Halo into *5xFAD ApoE KO* mice, which were treated with either PLX5622 or standard control chow. We observed increased MX04$^+$ aggregate formation only in the control chow-treated mice (Figure 4G), indicating that both APOE and microglia are necessary for MX04$^+$ aggregate formation.

Lysosomal dysfunction and pro-inflammatory activation promote APOE-induced MX04$^+$ aggregate formation in microglia

To explore whether we could reconstitute APOE-dependent MX04$^+$ aggregate formation in cell culture, we treated the microglial BV2 cell line with recombinant APOE and synthetic fluorophore-coupled Aβ-42 and visualized aggregate formation using MX04. Immunocytochemistry revealed a concentration-dependent formation of MX04$^+$ aggregates, which were positive for Aβ and APOE, 3 days after incubation (Figures 5A and S6A). Similar results were observed in primary microglia and human iPSC-derived microglia (Figures 5B, S6B, and S6C), but not with primary astrocytes (Figures S6D and S6E). BV2 cell lysates which contain MX04$^+$ aggregates displayed seeding activity when injected into *5xFAD* mice (Figures S6F and S6G).

Next, we asked how lysosomal function may modulate the aggregation process. When microglia were treated with compounds that interfere with lysosomal degradation (Lys05/chloroquine, bafilomycin, or leupeptin), we detected increased MX04$^+$ aggregate formation (Figures 5C, 5D, S6H, and S6I). To validate this finding *in vivo*, we conducted daily i.p. injections of chloroquine for 1 week in *5xFAD* mice and found an increase in MX04$^+$ aggregates in IBA1$^+$CD68$^+$ cells compared with controls (Figure 5E). Next, we explored the role of triggering receptor expressed on myeloid cells 2 (TREM2) in MX04$^+$ aggregate formation, which regulates the expression of genes related to lysosomal degradation.[13,42,43] We employed CRISPR-Cas9 to generate TREM2-deficient BV2 cells, conducted co-treatment experiments with APOE and Aβ-42, and observed an elevation in MX04$^+$ aggregate formation in TREM2-deficient BV2 cells compared with control cells (Figures 5C and S6J). To assess the *in vivo* relevance of these findings, we quantified MX04$^+$ aggregates co-localizing with CD68 in IBA1$^+$ cells in *APP/PS1 Trem2 KO*. Similarly to the results in cell culture, we observed an increase in the area and number of MX04$^+$ aggregates associated with CD68$^+$ immunostaining in *APP/PS1 Trem2 KO* compared with *APP/PS1* (Figures 5F, S6J, and S6K).

Activated interferon-responsive microglia have been identified in models of AD. We analyzed microglia in *5xFAD* mice for expression of signal transducer and activator of transcription 1 (STAT1 reactivity), a marker for interferon signal transduction activation. Co-labeling revealed that the majority of IBA1$^+$ cells were positive for both STAT1 and MX04 in the cortex of *5xFAD* mice, irrespective of the disease stage (Figure 6A). In addition, we detected STAT1$^+$IBA1$^+$ cells in direct contact to MX04$^+$ plaques and in the periplaque area. Next, we explored whether janus kinase/signal transducer and activator of transcription 1 (JAK/STAT1) inhibition could modulate the generation of β sheet-positive aggregates using the brain-permeable JAK/STAT1 inhibitor, baricitinib. We treated 6-week-old *5xFAD* mice with baricitinib for 12 weeks and analyzed plaque pathology by 3D light-sheet microscopy using Congo red staining at 4.5 months of age. We observed a reduction of Congo red$^+$ aggregates as compared with untreated controls (Figure 6B). Moreover, we found fewer STAT1$^+$IBA1$^+$ cells and fewer IBA1$^+$ cells with MX04$^+$ inclusions in *5xFAD* mice treated with baricitinib (Figure 6C). To further corroborate these findings, we generated *5xFAD* mice lacking STAT1 (*5xFAD Stat1 KO*) and performed 3D light-sheet microscopy using Congo red staining to determine the amyloid plaque load in the brain. We detected fewer Congo red$^+$ amyloid plaques in 3.5-month-old *5xFAD Stat1 KO* compared with *5xFAD* mice (Figure 6B). Next, we

(C) Left: representative image of MX04 (gray) CD68 (cyan) co-staining in IBA1$^+$ microglia (magenta) of male *5xFAD* mice with corresponding quantifications at different ages on the right. Data represent mean numbers and percentages ± SEM of MX04$^+$ IBA1$^+$ and MX04$^-$ IBA1$^+$ cells (3–4 mice per group). Right: representative images of MX04 (gray) CD68 (cyan) co-staining in IBA1$^+$ microglia of *APP/PS1* mice (12 months old) and *NL-G-F* mice (12 months old). Scale bar: original images, 10 μm and 3D reconstructions, 5 μm. See also Figure S5B.

(D) Representative images of APOE (yellow) Aβ (cyan) MX04 (gray) co-staining in IBA1$^+$ microglia (magenta) in human AD brain sections. Scale bar: 10 μm. See also Figure S5C.

(E) Representative EM images of fibrillary lysosomal aggregates (white arrows) in microglia of *5xFAD* mice (serial optical sections). Asterisk marks plaque core. Scale bar: 10 μm. See also Figure S5D.

(F) Left: schematic overview of PBS-extracted *5xFAD* brain lysate injection into microglia-depleted male *5xFAD* mice. Tile scan images and magnified images show MX04 (gray) labeling for plaque visualization in injected areas as well as IBA1 (magenta) and CD68 (cyan) staining. Scale bar: 50 μm. Right: quantification of MX04$^+$ aggregates in injected areas. Datapoints represent individual mice (n = 3), $^*p < 0.05$, $^{**}p < 0.01$, Student's t test, lines connecting the datapoints indicate the comparison to PBS-control-injected contralateral site.

(G) Left: schematic overview of purified soluble APOE-Halo injection experiments in microglia-depleted male *5xFAD ApoE*$^{-/-}$ mice. Tile scan images show the overview of injection areas in cortex. Magnified images show MX04 (gray) labeling for plaque visualization as well as IBA1 (magenta) and CD68 (cyan) staining. Scale bar: 50 μm. Right: quantification of MX04$^+$ aggregates. Datapoints represent individual mice (n = 3), $^*p < 0.05$, Student's t test.

Please cite this article in press as: Kaji et al., Apolipoprotein E aggregation in microglia initiates Alzheimer's disease pathology by seeding β-amyloidosis, Immunity (2024), https://doi.org/10.1016/j.immuni.2024.09.014

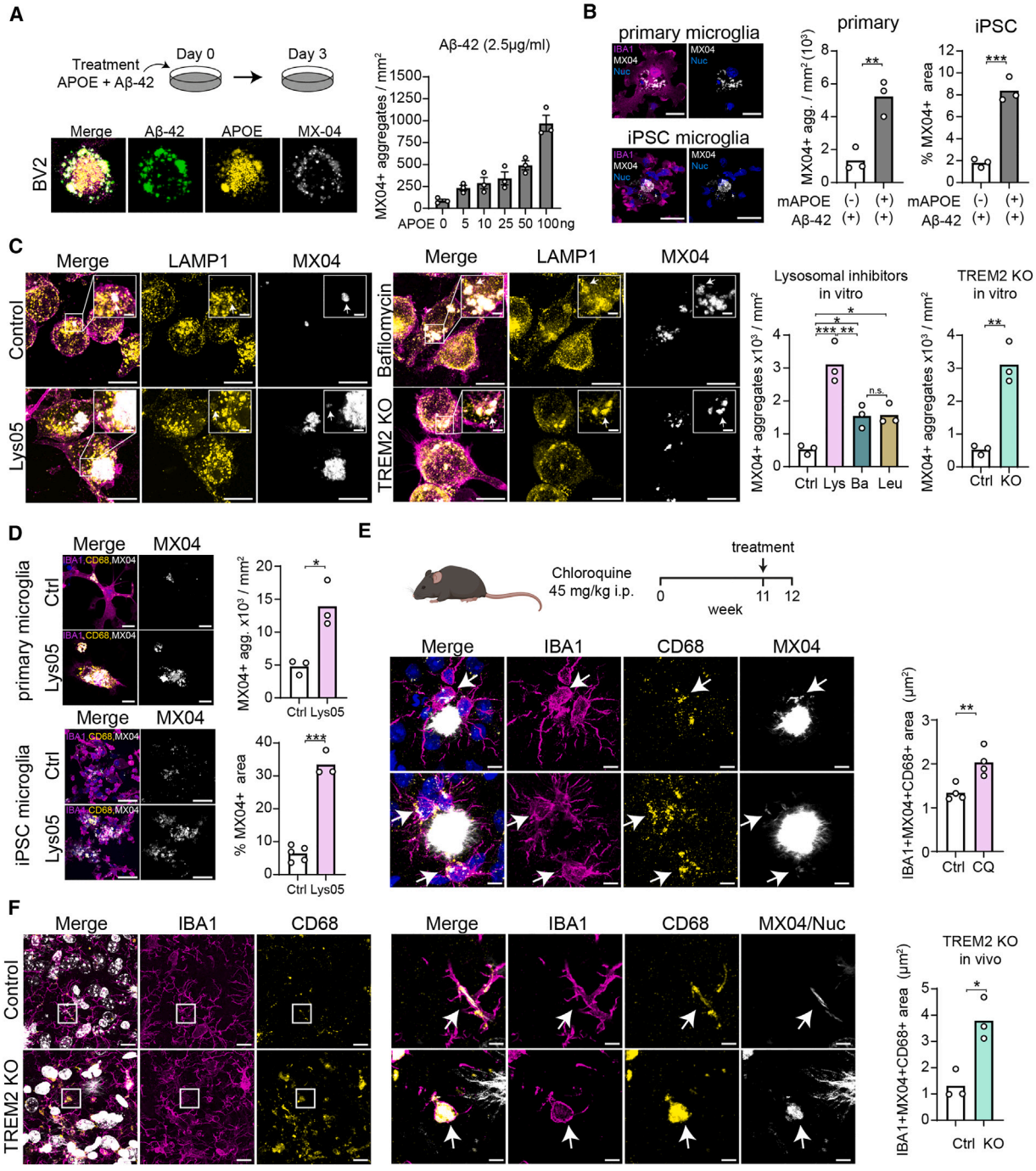

Figure 5. Lysosomal dysfunction promotes APOE-induced MX04⁺ aggregate formation in microglia

(A) Schematic overview and representative images of MX04⁺ aggregates induced by APOE/Aβ-42 co-treatment in BV2 cells. Quantification of MX04⁺ aggregates with increasing Aβ-42 or APOE concentrations. Datapoints represent individual cultures ($n = 3$) analyzed for mean numbers of MX04⁺ aggregates ± SEM. See also Figure S6A.

(B) Representative images of MX04⁺ (gray) aggregates induced by APOE/Aβ-42 co-treatment in primary microglia (scale bar: 10 μm) and iPSC microglia (scale bar: 25 μm) (IBA1⁺, magenta). Cells were incubated for 3 days with Aβ-42 (2.5 μg/mL) in the presence/absence of recombinant mouse APOE (100 ng/mL). Right: quantification of MX04⁺ aggregates. Datapoints represent individual cultures ($n = 3$) analyzed for mean numbers of MX04⁺ aggregates, $^{**}p < 0.01$, $^{***}p < 0.001$, Student's t test. See also Figures S6B–S6G.

(C) Representative images showing MX04⁺ (gray) aggregates co-stained with LAMP1 (yellow) in wild-type BV2 cells treated with lysosomal inhibitors and in TREM2 knockout BV-2 cells. Both cells were stained with IBA1 (magenta). Corresponding quantification of MX04⁺ aggregate numbers are shown on the right. Scale bar: 10 μm; inlets, 2 μm. Datapoints represent individual cultures ($n = 3$), $^{*}p < 0.05$, $^{**}p < 0.01$, $^{***}p < 0.001$, one-way ANOVA with Tukey's post hoc test. See also Figures S6H and S6J.

(legend continued on next page)

Please cite this article in press as: Kaji et al., Apolipoprotein E aggregation in microglia initiates Alzheimer's disease pathology by seeding β-amyloidosis, Immunity (2024), https://doi.org/10.1016/j.immuni.2024.09.014

explored JAK/STAT1 signaling in cell culture and found that the formation of MX04$^+$ aggregates by APOE and Aβ-42 co-treatment was associated with STAT1 activation, visualized by its translocation into the nucleus (Figures 6D and 6E). Notably, baricitinib reduced, while interferon-γ increased APOE- and Aβ-42-mediated MX04$^+$ aggregate formation (Figures 6F–6H). Together, these results suggest that lysosomal dysfunction and interferon activation promote APOE-induced MX04$^+$ aggregate formation in microglia.

Uptake of lipidated APOE particles into microglia enhances MX04$^+$ aggregate formation

Under physiological conditions, APOE is associated with lipids. Thus, we asked whether lipidated APOE particles could contribute to MX04$^+$ aggregate formation in microglia. We conducted a comparison between lipid-free recombinant APOE and APOE associated with lipids (1-palmitoyl-2-oleoyl-glycero-3-phosphocholine (POPC) and cholesterol) in our cell culture aggregation assay via co-incubation with Aβ-42. We found that lipidated APOE was taken up into cells more efficiently and enhanced MX04$^+$ aggregate formation (Figures 7A and 7B). In addition, physiological lipidated APOE particles isolated from human CSF were more potent in inducing MX04$^+$ aggregate formation compared with unlipidated recombinant hAPOE (Figures S7A–S7C). Lipidated APOE particles may undergo delipidation after entering the endo-lysosomal compartment, leading to the formation of lipid-depleted species that are prone to aggregation. To test this possibility, we generated APOE-Halo lipoprotein particles using a fluorescent cholesterol derivate (TMR-cholesterol). Using native gels, we were able to demonstrate the stable incorporation of TMR-cholesterol into lipoprotein particles (Figure S7D). We performed uptake assays in primary cultures of microglia and found transfer of TMR-cholesterol to PLIN2$^+$ lipid droplets already after 15–30 min (Figure S7E), suggesting that TMR-cholesterol rapidly dissociated from APOE-Halo-containing particles. Subsequently, we utilized a biochemical approach involving density gradient centrifugation to separate lipidated from unlipidated APOE-Halo and observed that the majority of APOE-Halo was recovered from the unlipidated fraction in cell extracts (Figure S7F). Next, we carried out the experiments using lipidated APOE3 and APOE4 and found that APOE4 was more efficient in inducing MX04$^+$ aggregates and in transferring TMR-cholesterol into the cells compared with APOE3 (Figures S7G–S7I).

Because these experiments indicated that APOE might be transported along with lipids into microglia, we reasoned that MX04$^+$IBA1$^+$ cells might accumulate cholesterol *in vivo*. To investigate this, we injected TMR-cholesterol into *5xFAD* mice, revealing TMR-cholesterol labeling in MX04$^+$CD68$^+$IBA1$^+$ cells (Figure 7C). We conducted fluorescence-activated cell sorting (FACS) to examine whether the cells had adapted their cholesterol metabolism in response to the increased cholesterol load. FACS was performed on YFP-expressing microglia, obtained from *5xFAD CX3CR1Cre-YFP* mice, and the cells were separated into MX04$^+$ and MX04$^-$ populations. By real-time quantitative PCR analysis of transcripts in cholesterol synthesis and uptake, we detected feedback inhibition of the cholesterol synthesis pathway and reduced expression of lipoprotein receptors in YFP$^+$MX04$^+$ cells, as one would predict after an increase in intracellular cholesterol load (Figure 7D). Gas chromatography-mass spectrometry analyses revealed a reduction of lanosterol, a precursor of cholesterol, in YFP$^+$MX04$^+$ compared with YFP$^+$MX04$^-$ cells (Figure 7D). The feedback inhibition of cholesterol synthesis in MX04$^+$ cells was replicated in cell culture (Figure 7E).

Because these experiments suggest a link between cholesterol metabolism, APOE uptake, and aggregate formation in microglia, we asked whether reducing cellular cholesterol synthesis would increase lipoprotein receptor expression, enhancing APOE uptake and aggregate formation *in vivo*. Because suppression of sterol synthesis represents an established concept for promoting lipoprotein uptake,[44] we devised a strategy for blocking *de novo* cholesterol synthesis in microglia. We used CRIPRS-Cas9 to generate BV2 cells that lack squalene synthase (*Fdft1*), an essential enzyme of the cholesterol biosynthesis pathway (Figures 7F and S7J). *Fdft1*-deficient cells cultured under low lipid conditions showed an upregulation of mRNA expression of several receptors related to APOE lipoprotein uptake (*Ldlr*, *Scarb1*, *CD36*). Notably, treatment with lipidated APOE and Aβ-42 was associated with an increase in MX04$^+$ aggregate formation in *Fdft1*-deficient BV2 as compared with control cells (Figure 7F).

Our finding that inhibition of microglial cholesterol synthesis enhances MX04$^+$ aggregation formation *in vitro* provided us with an experimental strategy for cell specific genetic experiments *in vivo*. To this end, we generated *5xFAD* mice lacking a functional sterol synthesis pathway in microglia (*FDFT1 KO 5xFAD*; *CX3CR1CreERT2 Fdft1*$^{flox/flox}$ *5xFAD*), which we compared with *5xFAD* control mice (*CX3CR1Cre 5xFAD*; *CX3CR1CreERT2 Fdft1*$^{wt/wt}$ *5xFAD*). 3D light-sheet microscopy revealed augmented plaque load in *FDFT1 KO 5xFAD* mice at 3.5 months of age (Figures 7G and S7K). In addition, we detected enhanced numbers of microglia with MX04$^+$ fibrillary morphology within the lysosomal compartment following cholesterol synthesis ablation (Figure 7G), providing evidence that cholesterol-deprived microglia promote Aβ amyloidosis.

DISCUSSION

We identified fibrillary aggregates of APOE, positive for β sheets dyes, in mice with Aβ amyloidosis and in human AD brain autopsy samples, and could show that they can serve as seeds

(D) Representative images showing MX04$^+$ (gray) aggregates in primary microglia (scale bar: 10 μm) and iPSC microglia (scale bar: 50 μm) after lysosomal inhibitor treatment. CD68 (yellow) and IBA1 (magenta) were co-stained. Corresponding quantification of MX04$^+$ aggregate numbers are shown on the right. Datapoints represent individual cultures (n = 3), $^*p < 0.05$, $^{***}p < 0.001$, Student's t test. See also Figure S6I.

(E) Top: schematic overview of chloroquine administration. Chloroquine or equal amount of saline was injected to female *5xFAD* mice intraperitoneally every day for 7 days, and mice were sacrificed on the following day after the final injection. Bottom: Representative images showing MX04$^+$ (gray) aggregates (arrows) in IBA1$^+$ (magenta) microglia, which were co-stained with CD68 (yellow). Quantification of IBA1$^+$/MX04$^+$/CD68$^+$ area. Datapoints represent individual mice (n = 4), $^{**}p < 0.01$, Student's t test.

(F) Representative images of sections from *APP/PS1 TREM2 KO* female mice compared with control (*APP/PS1*) (12 months old). Scale bar: 25 μm. Images with higher magnification (white square) show MX04$^+$ (gray) aggregates in CD68$^+$ (yellow) IBA1$^+$ (magenta) cells. Scale bar: 2.5 μm. Datapoints represent individual mice (n = 3) analyzed for mean area of MX04$^+$ aggregates in CD68$^+$IBA1$^+$ cells, $^*p < 0.05$, Student's t test. See also Figure S6K.

Please cite this article in press as: Kaji et al., Apolipoprotein E aggregation in microglia initiates Alzheimer's disease pathology by seeding β-amyloidosis, Immunity (2024), https://doi.org/10.1016/j.immuni.2024.09.014

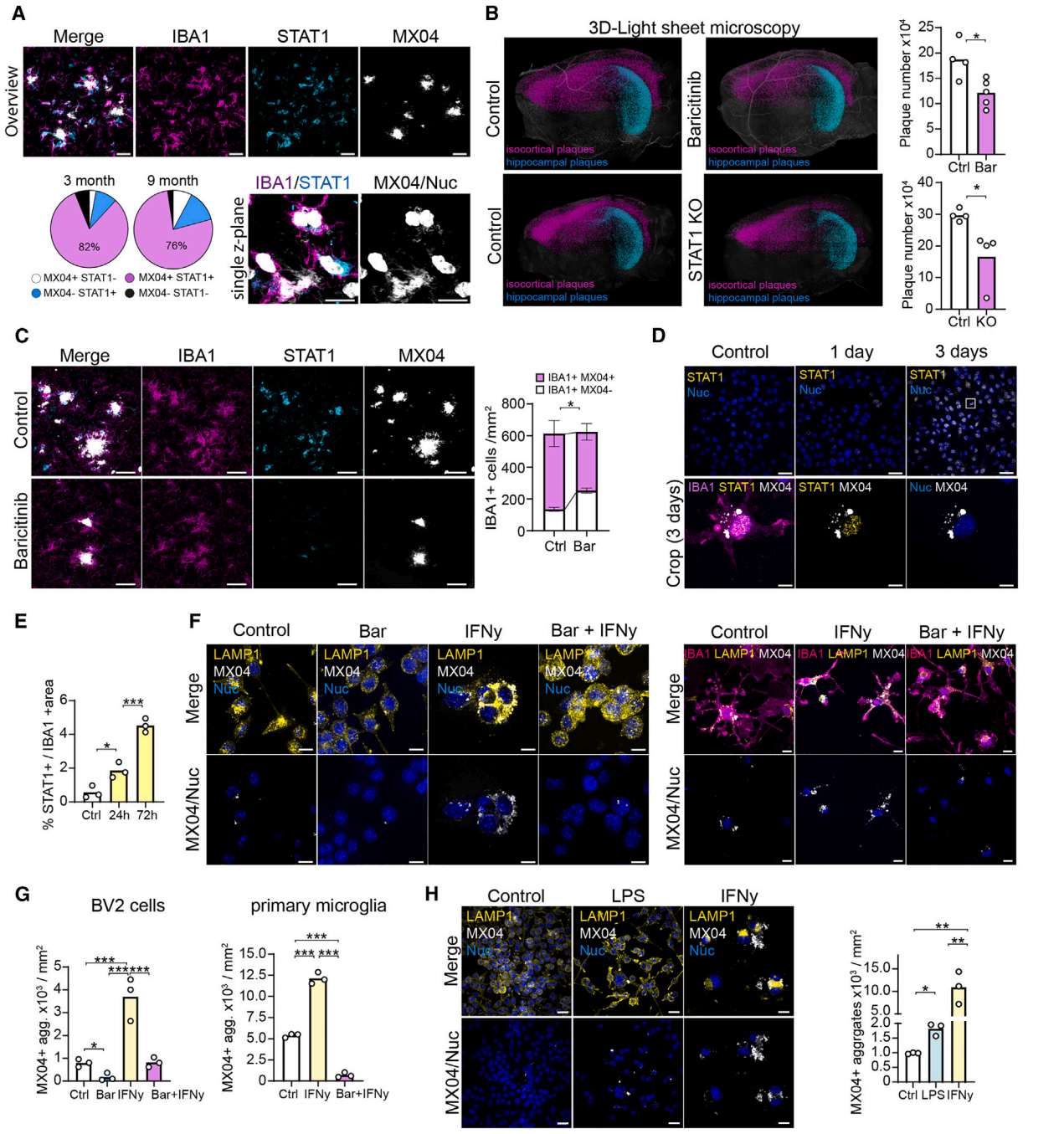

Figure 6. Microglial JAK/STAT1 inhibition reduces amyloid pathology

(A) Top: representative images of STAT1$^+$ (cyan) IBA1$^+$ (magenta) cells in 6-month-old male *5xFAD* mice (scare bar, 20 μm). Bottom right: magnified views showing STAT1$^+$MX04$^+$ cells. Scale bar: 10 μm. Pie chart shows the mean percentages of total IBA1$^+$ cells positive or negative for STAT1 and/or MX04 at 3 and 9 months of age (3–4 mice for each age).

(B) Top: representative 3D light-sheet microscopy images of male *5xFAD* mice (4.5 months old) treated with baricitinib or control with corresponding quantification on the right. Bottom, representative 3D light-sheet microscopy images of *5xFAD* mice and *5xFAD STAT1 KO* mice (3.5 months old, females). Cortical plaques are shown in magenta and hippocampal plaques in cyan. Datapoints represent individual mice (n = 4–5) analyzed for mean numbers of Congo red$^+$ aggregates, $^*p < 0.05$, Student's t test.

(C) Representative images showing STAT1$^+$ (cyan) MX04$^+$ (gray) IBA1+ (magenta) cells in male *5xFAD* mice (4.5 months old) treated with baricitinib or controls with corresponding quantification on the right. Scale bar: 20 μm. Data represent individual mean numbers of MX04$^+$ or MX04$^-$ IBA1$^+$ cells ± SEM (3 mice per group), $^*p < 0.05$, Student's t test.

(D) Top: representative images of STAT1$^+$ (yellow) BV2 cells 24 and 72 h after incubation with APOE (100 ng/mL) and Aβ-42 (2.5 μg/mL). Scale bar: 25 μm. Bottom: representative images of MX04$^+$ (gray) aggregates in STAT1$^+$ (yellow) IBA1$^+$ (magenta) primary microglia 72 h after treatment. Scale bar: 5 μm.

(legend continued on next page)

for Aβ amyloidosis in mice. In addition, we provide evidence that the aggregation process can occur within the endo-lysosomal system of microglia and is modulated by immune and lipid metabolism. We propose that the upregulation of APOE expression, as it occurs in AD, may lead to enhanced uptake of lipoprotein particles within microglia where a pathological cascade culminating in Aβ amyloidosis is initiated.

How does this align with previous research? Microglia are known to play a critical role in the defense against AD pathology, combating both neurofibrillary tangle and amyloid plaque accumulation.[45–47] When these defensive functions of microglia are compromised, there is an increase in the accumulation of amyloid plaques, demonstrating a role of microglia in Aβ clearance.[48,49] Ablation of microglia, for example, by using brain-penetrant CSF1R inhibitor or by employing the CD11b-herpes simplex virus thymidine kinase mouse model crossed to AD mouse models, has shown no effect on amyloid plaque formation and maintenance.[50,51] In contrast to this view, other investigators discovered that depleting microglia can impede Aβ plaque formation.[52,53] These discrepancies could be attributed to microglia being depleted at various stages of the disease, which are known to be associated with distinct phases of the amyloid growth process. Thus, one may reconcile these opposing views on microglia by proposing distinct functions in Aβ amyloidosis. It is possible that microglia are responsible for both the generation and degradation of Aβ plaques, which may occur simultaneously within the lysosomal compartment. During the nucleation stage, when small aggregates are forming, the microglial endo-lysosomal system may have detrimental function by providing a seeding platform for amyloidosis. This injurious cascade may begin when indigestible, compacted material is starting to form within lysosomes. However, once enough seeds have been produced, the degradative and clearance functions of microglia are anticipated to take over. In line with a function of microglia in amyloid plaque biogenesis, microglia deficient for the two TAM receptor tyrosine kinases, AXL and MER, that are unable to internalize Aβ plaque develop fewer dense-core plaque.[54] Taken together with our results, one can propose that phagocytosed Aβ can undergo compaction within lysosomes, facilitated by the function of APOE, resulting in the formation of dense-core material. These densely packed, degradation-resistant aggregates could be released from microglia into the extracellular space via either exocytosis or microglial death, thereby driving the growth of dense-core amyloid plaques.

What could be the mechanisms for the pathogenic protein seeding by APOE? APOE can form tetrameric species and even higher molecular aggregates or protofibrils that bind the amyloid dyes Thioflavin T and Congo red *in vitro*.[38] Consistent with this previous work, we find that purified APOE obtained from an AD mouse model or from human AD brains, as well as recombinantly produced APOE aggregates, stain positive for amyloid dyes and appear with irregular protofilament-like morphology but are distinct from classical amyloid. These APOE aggregates appear to be able to self-replicate, as shown by Thioflavin T fibrillation assay, and to serve as templates for Aβ growth *in vitro* and *in vivo*. These findings concur with a role of APOE, and in particular APOE4 in Aβ aggregation.[55–58] Distinct misfolded proteins can synergize in a heterologous fashion, accelerating amyloid fiber assembly.[59,60] One underlying mechanism for this coupling is cross-seeding of protein aggregation, which occurs when one misfolded protein can promote the polymerization of another. It is possible that APOE aggregates provide a surface for the nucleation and/or growth of Aβ. Such a mechanism may work in both directions, accelerating the growth of both APOE and Aβ aggregates. Indirect mechanisms such as impairment of cellular or lysosomal integrity or enhancement of oxidative stress or inflammatory responses that enhance the replication process are also feasible. This could, for example, explain the enhanced seeding of amyloid in TREM2-deficient mice in which lysosomal degradative function is impaired.[61] Our results indicate that phagocytosis of APOE and Aβ aggregates initiates an interferon response, which amplifies the aggregation process. The interferon-mediated signaling pathway in microglia has previously been shown to be integral to neuroinflammation and neuropathology in AD.[12,62–66] One possible explanation could be the role of interferon-stimulated genes in lysosomal remodeling.[67] As the disease progresses, microglia may eventually transition into a state resembling exhaustion, characterized by terminal inflammation.[68]

Limitations of the study

Using mouse models with genetically engineered familial AD mutations has limitations when studying the biology of APOE, a risk factor for sporadic AD. Additionally, humanized APOE3 and APOE4 knockin mice face challenges because it is uncertain how well these proteins recognize mouse receptors. There are also technological limitations. Despite extensive validation to ensure the HaloTag does not interfere with APOE's normal function, this cannot be entirely ruled out. Moreover, our treatments to interfere with interferon signaling are not specific to microglia and may only indirectly affect these cells. Lastly, our analysis of human samples is constrained by small sample sizes. Therefore, further research is needed to determine if the mechanisms described in this paper apply to sporadic AD in humans.

(E) Corresponding quantification for (D). Datapoints represent individual cultures (n = 3) analyzed for mean percentages of STAT1$^+$ per IBA1$^+$ area, $^*p < 0.05$, $^{***}p < 0.001$, one-way ANOVA with Tukey's post hoc test.

(F) Left: representative images of MX04$^+$ aggregates (gray) in STAT1$^+$ (yellow) BV2 cells, which were incubated for 72 h with baricitinib and/or interferon gamma (IFN-γ) together with APOE/Aβ-42. Nuclear labeling was performed with Hoechst (blue). Scale bar: 10 μm. Right: representative images of MX04$^+$ aggregates (gray) in LAMP1$^+$ (yellow) IBA1$^+$ (magenta) primary microglia, which were incubated with baricitinib and/or interferon gamma (IFN-γ) together with APOE/Aβ-42. Nuclear labeling was performed with Hoechst (blue). Scale bar: 10 μm.

(G) Quantification of MX04$^+$ aggregates in (F). Datapoints represent individual cultures (n = 3) analyzed for numbers of MX04$^+$ aggregates, $^{***}p < 0.001$, by one-way ANOVA with Tukey's post hoc test.

(H) Representative images of MX04$^+$ aggregates (gray) in STAT1$^+$ (yellow) BV2 cells, treated for 72 h with either lipopolysaccharide (LPS) or IFN-γ together with APOE/Aβ-42 (scale bar, 10 μm) with corresponding quantification on the right. Datapoints represent individual cultures (n = 3) analyzed for numbers of MX04$^+$ aggregates, $^*p < 0.05$, $^{**}p < 0.01$, one-way ANOVA with Tukey's post hoc test.

Please cite this article in press as: Kaji et al., Apolipoprotein E aggregation in microglia initiates Alzheimer's disease pathology by seeding β-amyloidosis, Immunity (2024), https://doi.org/10.1016/j.immuni.2024.09.014

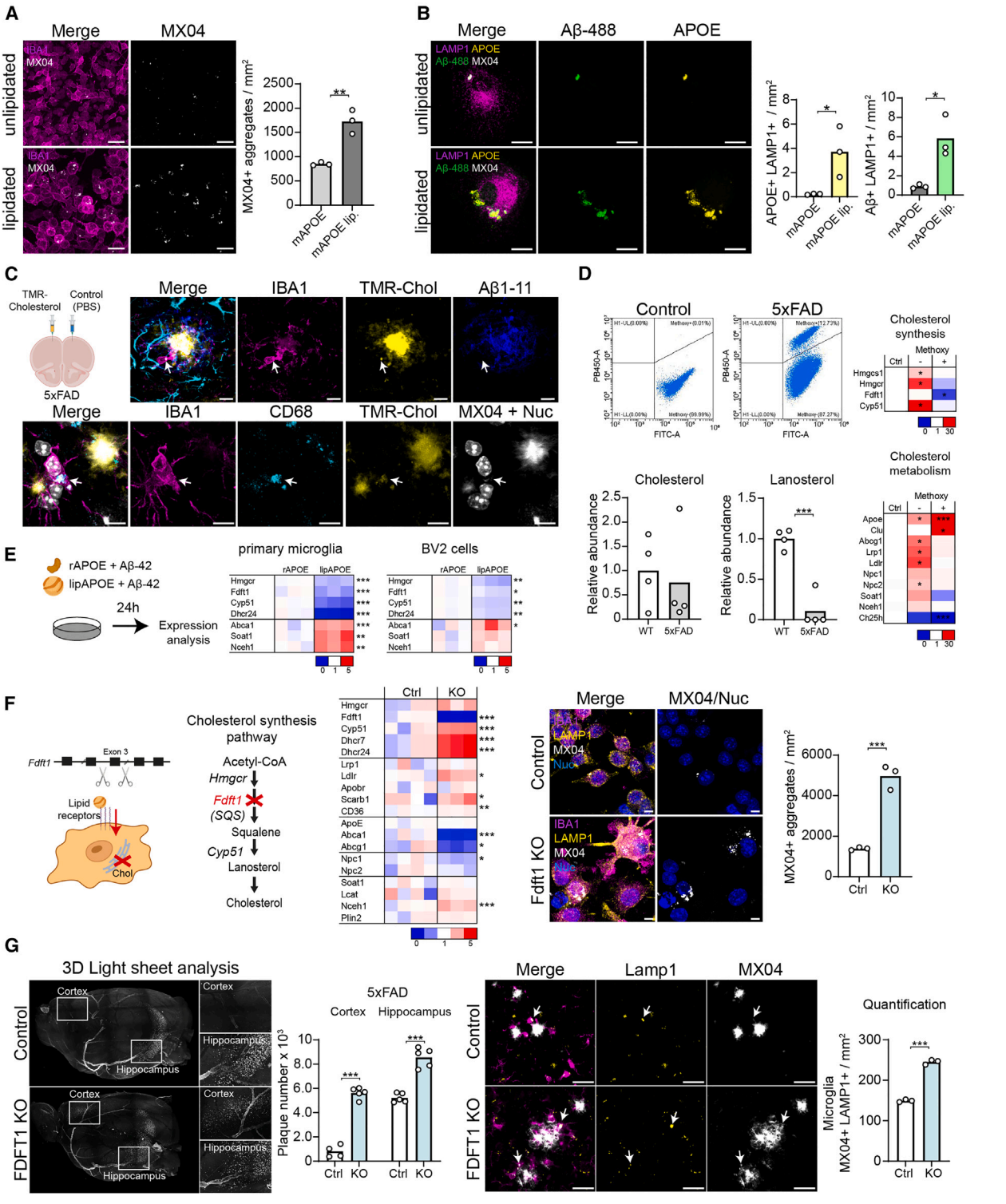

Figure 7. Uptake of lipidated APOE particles into microglia enhances MX04⁺ aggregate formation

(A) Representative images of MX04⁺ (gray) aggregates in IBA1⁺ (magenta) BV2 cells 72 h after treatment with either POPC/cholesterol-lipidated mouse APOE + Aβ-42 or unlipidated mouse APOE + Aβ-42 with corresponding quantification on the right. Scale bar: 20 μm. Datapoints represent individual cultures (n = 3) analyzed for mean numbers of MX04⁺ aggregates, $^{**}p < 0.01$, Student's t test. See also Figures S7A–S7C.

(B) Representative images of internalized Aβ-488 (green) and APOE (His, yellow) in IBA1⁺ (magenta) BV2 cells incubated for 4 h with lipidated mouse APOE + Aβ-42 or unlipidated mouse APOE + Aβ-42. Scale bar: 10 μm. Uptake of N-terminally His-tagged recombinant mouse APOE was evaluated by His-tag staining. Datapoints represent individual cultures (n = 3) analyzed for numbers of MX04⁺ aggregates, $^{*}p < 0.05$, Student's t test. See also Figures S7D–S7I.

(legend continued on next page)

Please cite this article in press as: Kaji et al., Apolipoprotein E aggregation in microglia initiates Alzheimer's disease pathology by seeding β-amyloidosis, Immunity (2024), https://doi.org/10.1016/j.immuni.2024.09.014

RESOURCE AVAILABILITY

Lead contact

Further information and requests for resources and reagents should be directed to and will be fulfilled by the lead contact, Mikael Simons (mikael.simons@dzne.de).

Materials availability

Reagents generated in this study are available from the lead contact with a completed Material Transfer Agree.

Data and code availability

- All data reported in this paper will be shared by the lead contact upon request.
- This study did not generate any code.
- Any additional information required to reanalyze the data reported in this paper is available from the lead contact upon request.

ACKNOWLEDGMENTS

The work was supported by grants from the German Research Foundation (TRR274-1, SyNergy Excellence Cluster, EXC2145, Projekt ID 390857198, Koselleck Project HA1737/16-1 [to C.H.]), Chan Zuckerberg Initiative, Collaborative Pairs grants (to M.G. and M. Simons), the ERC (Advanced Grant to M. Simons), the Alzheimer Förderungs Initiative (to L. Spieth and G.S.) and the Adelson Medical Research Foundation. L.H. is supported by the Klaus Faber Stiftung and S. Kajiiz by the Uehara Memorial Foundation and Grant-in-Aid for Young Scientists (B) (19 K16915) from the Japan Society for the Promotion of Science (JSPS). We thank Dr. Feng Zhang (Broad Institute) for providing PX458. We thank C. Müller, G. Kislinger, C. Niemann, A.M. Bernhardt, B.Ö. Haciahmet, B. Nuscher, A. Reifschneider, K. Buschmann, G. Werner, C. Giudici, N. Blomberg, L. Huber, Y. Nihei, and M. Hasegawa for helpful suggestions or technical assistance.

AUTHOR CONTRIBUTIONS

S. Kaji, S.A.B., L. Spieth, G.S., and M. Simons conceived the project and designed experiments. S. Kaji, S.A.B., L. Spieth, A.O.S., S. Kedia, L. Schlaphoff, M.Z., T.N., A.D., S.V., L.H., C.D., P.S., D.E., B.W., and L.B. carried out experiments. S. Kaji, S.A.B., L. Spieth, A.O.S., S. Kedia, L. Schlaphoff, M.Z., T.N., A.D., S.V., L.H., C.D., G.W., P.S., D.E., B.W., F.K., M.G., T.I., W.W., M. Schifferer, M.W., K.-A.N., C.H., T.A., S.J., G.S., M. Simons, and O.W. analyzed the data or supervised data acquisition or analysis. S. Kaji, S.A.B., and L. Spieth visualized the data, and M. Simons wrote the manuscript with input from all authors.

DECLARATION OF INTERESTS

C.H. has collaboration contract with Denali for the development of TREM2 agonists.

STAR★METHODS

Detailed methods are provided in the online version of this paper and include the following:

- KEY RESOURCES TABLE
- EXPERIMENTAL MODEL AND STUDY PARTICIPANT DETAILS
  - Human autopsy samples
  - Cell lines and primary cells
  - Mice
- METHOD DETAILS
  - Mice
  - Generation of APOE-Halo reporter mice
  - Treatments to mice
  - Serum analysis
  - Cholesterol ester analysis by mass spectrometry
  - Isolation of serum and brain APOE-Halo from *ApoE-Halo* mice for EM analysis
  - Isolation of MX04$^+$ microglia in *5xFAD* mice
  - mRNA expression analysis
  - Sterol measurements
  - Generation of BV2 *FDFT1* and *TREM2* knockouts
  - Generation of iPSC derived microglia cells
  - Aggregation assay in cell culture
  - Preparation of amyloid protein extracts in mouse brains by DEA/RIPA/FA
  - Western Blot
  - Isolation of sarkosyl-insoluble fractions and PBS extracted lysate
  - APOE aggregate isolation from *ApoE-Halo 5xFAD* mouse and human brain
  - Isolation of brain-derived RIPA-soluble APOE-Halo from *ApoE-Halo* mouse
  - Preparation of BV2 cell lysate for stereotactic injection

(C) Injection of TMR-cholesterol (TMR-Chol) injection into 6-month-old *5xFAD* mice. Top: representative images of TMR-Chol$^+$ (yellow) Aβ$^+$ (blue) plaques around IBA1$^+$ (magenta) cells. Scale bar: 10 μm. Bottom: representative images of TMR-Chol$^+$ (yellow) MX04$^+$ (gray) aggregates in CD68$^+$ (cyan) IBA1$^+$ (magenta) cells. Scale bar: 10 μm.

(D) Top left: CD11b$^+$ magnetic activated cell sorting and subsequent flow cytometry cell sorting for isolation of MX04$^+$ and MX04$^-$ cells from 8-month-old male *5xFAD* and wild-type control mice (n = 4). Top right and bottom right: quantitative PCR (qPCR) analysis of transcripts involved in cholesterol synthesis and metabolism in MX04$^-$ and MX04$^+$ cells from *5xFAD* mice and those in MX04$^-$ cells from wild-type control. Heatmaps represent mean expression as fold-change to control (3 mice per group), $^*p < 0.05$, $^{***}p < 0.001$, one-way ANOVA with Tukey's post hoc test. Bottom left: gas chromatography-mass spectrometry (GC-MS) measurements of cholesterol and lanosterol of CD11b$^+$ sorted cells from wild-type and *5xFAD* mice (6 months old), n = 4, $^{***}p < 0.001$, Student's t test.

(E) qPCR analysis of transcripts in cholesterol synthesis and transport in primary microglia and BV2 cells 24 h after treatment with lipidated APOE + Aβ-42 or unlipidated APOE + Aβ-42. Heatmaps represent individual expression as fold-change to unlipidated condition, n = 3 cultures, $^*p < 0.05$, $^{**}p < 0.01$, $^{***}p < 0.001$, one-way ANOVA with Tukey's post hoc test.

(F) Left: schematic overview of generation of *Fdft1* Exon 3 knockout BV2 cells (*Fdft1*-deficient BV2 cells), defective in cholesterol synthesis. Cells were collected for RNA analysis after 4 h of serum starvation. Middle: qPCR analysis of transcripts in cholesterol synthesis and metabolism and transport in control BV2 and *Fdft1*-deficient BV2 cells. Heatmaps represent individual expression as fold-change to control, n = 3–4 independent cultures, $^*p < 0.05$, $^{**}p < 0.01$, $^{***}p < 0.001$, one-way ANOVA with Tukey's post hoc test. Right: representative images of MX04$^+$ aggregates (gray) in LAMP1$^+$ (yellow) IBA1$^+$ (magenta) *Fdft1*-deficient and control BV2 cells 72 h after incubation with lipidated APOE + Aβ-42. Scale bar: 10 μm. Datapoints represent individual cultures (n = 3) analyzed for mean numbers of MX04$^+$ aggregates, $^{***}p < 0.001$, Student's t test. See also Figure S7J.

(G) Left: plaque analysis by 3D light-sheet microscopy in *CX3CR1CreERT2 FDFT1*$^{flox/flox}$ *5xFAD* (*FDFT1 KO 5xFAD*) and corresponding controls *CX3CR1CreERT2 FDFT1*$^{wt/wt}$ *5xFAD* (*CX3CR1Cre 5xFAD*) mice (3.5 months old, males) with corresponding quantification on the right. Representative images show Congo red$^+$ (orange) plaques in the isocortex and hippocampus. Datapoints represent individual mice (n = 5) analyzed for mean numbers of plaques in cortex and hippocampus, $^{***}p < 0.001$, Student's t test. Right: representative images of MX04$^+$ aggregates (gray) in LAMP1$^+$ (yellow) IBA1$^+$ (magenta) cells of *CX3CR1Cre 5xFAD* and *FDFT1 KO 5xFAD* mice (3.5 months old) with corresponding quantification on the right. Scale bar: 25 μm. Datapoints represent individual mice (n = 3) analyzed for mean numbers of MX04$^+$ LAMP1$^+$ aggregates, $^{***}p < 0.001$, Student's t test. See also Figure S7K.

SUPPLEMENTAL INFORMATION

Supplemental information can be found online at https://doi.org/10.1016/j.immuni.2024.09.014.

Received: June 8, 2023
Revised: February 9, 2024
Accepted: September 17, 2024
Published: October 16, 2024

REFERENCES

1. Scheltens, P., De Strooper, B., Kivipelto, M., Holstege, H., Chételat, G., Teunissen, C.E., Cummings, J., and van der Flier, W.M. (2021). Alzheimer's disease. Lancet *397*, 1577–1590. https://doi.org/10.1016/S0140-6736(20)32205-4.
2. De Strooper, B., and Karran, E. (2016). The cellular phase of Alzheimer's disease. Cell *164*, 603–615. https://doi.org/10.1016/j.cell.2015.12.056.
3. Haass, C., and Selkoe, D.J. (2007). Soluble protein oligomers in neurodegeneration: lessons from the Alzheimer's amyloid beta-peptide. Nat. Rev. Mol. Cell Biol. *8*, 101–112. https://doi.org/10.1038/nrm2101.
4. Jucker, M., and Walker, L.C. (2013). Self-propagation of pathogenic protein aggregates in neurodegenerative diseases. Nature *501*, 45–51. https://doi.org/10.1038/nature12481.
5. Aguzzi, A., and O'Connor, T. (2010). Protein aggregation diseases: pathogenicity and therapeutic perspectives. Nat. Rev. Drug Discov. *9*, 237–248. https://doi.org/10.1038/nrd3050.
6. Hardy, J., and Selkoe, D.J. (2002). The amyloid hypothesis of Alzheimer's disease: progress and problems on the road to therapeutics. Science *297*, 353–356. https://doi.org/10.1126/science.1072994.
7. Prusiner, S.B. (1998). Prions. Proc. Natl. Acad. Sci. USA *95*, 13363–13383. https://doi.org/10.1073/pnas.95.23.13363.
8. Sadick, J.S., O'Dea, M.R., Hasel, P., Dykstra, T., Faustin, A., and Liddelow, S.A. (2022). Astrocytes and oligodendrocytes undergo subtype-specific transcriptional changes in Alzheimer's disease. Neuron *110*, 1788–1805.e10. https://doi.org/10.1016/j.neuron.2022.03.008.
9. Chen, W.T., Lu, A., Craessaerts, K., Pavie, B., Sala Frigerio, C., Corthout, N., Qian, X., Laláková, J., Kühnemund, M., Voytyuk, I., et al. (2020). Spatial transcriptomics and in situ sequencing to study Alzheimer's disease. Cell *182*, 976–991.e19. https://doi.org/10.1016/j.cell.2020.06.038.
10. Habib, N., McCabe, C., Medina, S., Varshavsky, M., Kitsberg, D., Dvir-Szternfeld, R., Green, G., Dionne, D., Nguyen, L., Marshall, J.L., et al. (2020). Disease-associated astrocytes in Alzheimer's disease and aging. Nat. Neurosci. *23*, 701–706. https://doi.org/10.1038/s41593-020-0624-8.
11. Jansen, I.E., Savage, J.E., Watanabe, K., Bryois, J., Williams, D.M., Steinberg, S., Sealock, J., Karlsson, I.K., Hägg, S., Athanasiu, L., et al. (2019). Genome-wide meta-analysis identifies new loci and functional pathways influencing Alzheimer's disease risk. Nat. Genet. *51*, 404–413. https://doi.org/10.1038/s41588-018-0311-9.
12. Sala Frigerio, C., Wolfs, L., Fattorelli, N., Thrupp, N., Voytyuk, I., Schmidt, I., Mancuso, R., Chen, W.T., Woodbury, M.E., Srivastava, G., et al. (2019). The major risk factors for Alzheimer's disease: age, sex, and genes modulate the microglia response to Abeta plaques. Cell Rep. *27*, 1293–1306.e6. https://doi.org/10.1016/j.celrep.2019.03.099.
13. Keren-Shaul, H., Spinrad, A., Weiner, A., Matcovitch-Natan, O., Dvir-Szternfeld, R., Ulland, T.K., David, E., Baruch, K., Lara-Astaiso, D., Toth, B., et al. (2017). A unique microglia type associated with restricting development of Alzheimer's disease. Cell *169*, 1276–1290.e17. https://doi.org/10.1016/j.cell.2017.05.018.
14. Efthymiou, A.G., and Goate, A.M. (2017). Late onset Alzheimer's disease genetics implicates microglial pathways in disease risk. Mol. Neurodegener. *12*, 43. https://doi.org/10.1186/s13024-017-0184-x.
15. Krasemann, S., Madore, C., Cialic, R., Baufeld, C., Calcagno, N., El Fatimy, R., Beckers, L., O'Loughlin, E., Xu, Y., Fanek, Z., et al. (2017). The TREM2-APOE pathway drives the transcriptional phenotype of dysfunctional microglia in neurodegenerative diseases. Immunity *47*, 566–581.e9. https://doi.org/10.1016/j.immuni.2017.08.008.
16. Matarin, M., Salih, D.A., Yasvoina, M., Cummings, D.M., Guelfi, S., Liu, W., Nahaboo Solim, M.A., Moens, T.G., Paublete, R.M., Ali, S.S., et al. (2015). A genome-wide gene-expression analysis and database in transgenic mice during development of amyloid or tau pathology. Cell Rep. *10*, 633–644. https://doi.org/10.1016/j.celrep.2014.12.041.
17. Wightman, D.P., Jansen, I.E., Savage, J.E., Shadrin, A.A., Bahrami, S., Holland, D., Rongve, A., Børte, S., Winsvold, B.S., Drange, O.K., et al. (2021). A genome-wide association study with 1,126,563 individuals identifies new risk loci for Alzheimer's disease. Nat. Genet. *53*, 1276–1282. https://doi.org/10.1038/s41588-021-00921-z.
18. Chen, Y., Strickland, M.R., Soranno, A., and Holtzman, D.M. (2021). Apolipoprotein E: structural insights and links to Alzheimer disease pathogenesis. Neuron *109*, 205–221. https://doi.org/10.1016/j.neuron.2020.10.008.
19. Yamazaki, Y., Zhao, N., Caulfield, T.R., Liu, C.C., and Bu, G. (2019). Apolipoprotein E and Alzheimer disease: pathobiology and targeting strategies. Nat. Rev. Neurol. *15*, 501–518. https://doi.org/10.1038/s41582-019-0228-7.
20. Koutsodendris, N., Nelson, M.R., Rao, A., and Huang, Y. (2022). Apolipoprotein E and Alzheimer's disease: findings, hypotheses, and potential mechanisms. Annu. Rev. Pathol. *17*, 73–99. https://doi.org/10.1146/annurev-pathmechdis-030421-112756.
21. Rebeck, G.W. (2017). The role of APOE on lipid homeostasis and inflammation in normal brains. J. Lipid Res. *58*, 1493–1499. https://doi.org/10.1194/jlr.R075408.
22. Ladu, M.J., Reardon, C., Van Eldik, L., Fagan, A.M., Bu, G., Holtzman, D., and Getz, G.S. (2000). Lipoproteins in the central nervous system. Ann. N. Y. Acad. Sci. *903*, 167–175. https://doi.org/10.1111/j.1749-6632.2000.tb06365.x.
23. Ioannou, M.S., Jackson, J., Sheu, S.H., Chang, C.L., Weigel, A.V., Liu, H., Pasolli, H.A., Xu, C.S., Pang, S., Matthies, D., et al. (2019). Neuron-astrocyte metabolic coupling protects against activity-induced fatty acid toxicity. Cell *177*, 1522–1535.e14. https://doi.org/10.1016/j.cell.2019.04.001.
24. Blanchard, J.W., Akay, L.A., Davila-Velderrain, J., von Maydell, D., Mathys, H., Davidson, S.M., Effenberger, A., Chen, C.Y., Maner-Smith, K., Hajjar, I., et al. (2022). APOE4 impairs myelination via cholesterol dysregulation in oligodendrocytes. Nature *611*, 769–779. https://doi.org/10.1038/s41586-022-05439-w.
25. Camargo, N., Goudriaan, A., van Deijk, A.F., Otte, W.M., Brouwers, J.F., Lodder, H., Gutmann, D.H., Nave, K.A., Dijkhuizen, R.M., Mansvelder, H.D., et al. (2017). Oligodendroglial myelination requires astrocyte-derived lipids. PLoS Biol. *15*, e1002605. https://doi.org/10.1371/journal.pbio.1002605.

26. Saher, G., Brügger, B., Lappe-Siefke, C., Möbius, W., Tozawa, R., Wehr, M.C., Wieland, F., Ishibashi, S., and Nave, K.A. (2005). High cholesterol level is essential for myelin membrane growth. Nat. Neurosci. *8*, 468–475. https://doi.org/10.1038/nn1426.

27. Mauch, D.H., Nägler, K., Schumacher, S., Göritz, C., Müller, E.C., Otto, A., and Pfrieger, F.W. (2001). CNS synaptogenesis promoted by glia-derived cholesterol. Science *294*, 1354–1357. https://doi.org/10.1126/science.294.5545.1354.

28. Serrano-Pozo, A., Das, S., and Hyman, B.T. (2021). APOE and Alzheimer's disease: advances in genetics, pathophysiology, and therapeutic approaches. Lancet Neurol. *20*, 68–80. https://doi.org/10.1016/S1474-4422(20)30412-9.

29. DeMattos, R.B., Cirrito, J.R., Parsadanian, M., May, P.C., O'Dell, M.A., Taylor, J.W., Harmony, J.A.K., Aronow, B.J., Bales, K.R., Paul, S.M., et al. (2004). ApoE and clusterin cooperatively suppress Abeta levels and deposition: evidence that ApoE regulates extracellular Abeta metabolism in vivo. Neuron *41*, 193–202. https://doi.org/10.1016/s0896-6273(03)00850-x.

30. Holtzman, D.M., Fagan, A.M., Mackey, B., Tenkova, T., Sartorius, L., Paul, S.M., Bales, K., Ashe, K.H., Irizarry, M.C., and Hyman, B.T. (2000). Apolipoprotein E facilitates neuritic and cerebrovascular plaque formation in an Alzheimer's disease model. Ann. Neurol. *47*, 739–747. https://doi.org/10.1002/1531-8249(200006)47:6<739::AID-ANA6>3.0.CO;2-8.

31. Bales, K.R., Verina, T., Dodel, R.C., Du, Y., Altstiel, L., Bender, M., Hyslop, P., Johnstone, E.M., Little, S.P., Cummins, D.J., et al. (1997). Lack of apolipoprotein E dramatically reduces amyloid beta-peptide deposition. Nat. Genet. *17*, 263–264. https://doi.org/10.1038/ng1197-263.

32. Takacs, C.N., Andreo, U., Belote, R.L., Pulupa, J., Scull, M.A., Gleason, C.E., Rice, C.M., and Simon, S.M. (2017). Green fluorescent protein-tagged apolipoprotein E: A useful marker for the study of hepatic lipoprotein egress. Traffic *18*, 192–204. https://doi.org/10.1111/tra.12467.

33. Xu, Q., Bernardo, A., Walker, D., Kanegawa, T., Mahley, R.W., and Huang, Y. (2006). Profile and regulation of apolipoprotein E (ApoE) expression in the CNS in mice with targeting of green fluorescent protein gene to the ApoE locus. J. Neurosci. *26*, 4985–4994. https://doi.org/10.1523/JNEUROSCI.5476-05.2006.

34. Oakley, H., Cole, S.L., Logan, S., Maus, E., Shao, P., Craft, J., Guillozet-Bongaarts, A., Ohno, M., Disterhoft, J., Van Eldik, L., et al. (2006). Intraneuronal beta-amyloid aggregates, neurodegeneration, and neuron loss in transgenic mice with five familial Alzheimer's disease mutations: potential factors in amyloid plaque formation. J. Neurosci. *26*, 10129–10140. https://doi.org/10.1523/JNEUROSCI.1202-06.2006.

35. Namba, Y., Tomonaga, M., Kawasaki, H., Otomo, E., and Ikeda, K. (1991). Apolipoprotein E immunoreactivity in cerebral amyloid deposits and neurofibrillary tangles in Alzheimer's disease and kuru plaque amyloid in Creutzfeldt-Jakob disease. Brain Res. *541*, 163–166. https://doi.org/10.1016/0006-8993(91)91092-f.

36. Yang, Y., Arseni, D., Zhang, W., Huang, M., Lövestam, S., Schweighauser, M., Kotecha, A., Murzin, A.G., Peak-Chew, S.Y., Macdonald, J., et al. (2022). Cryo-EM structures of amyloid-beta 42 filaments from human brains. Science *375*, 167–172. https://doi.org/10.1126/science.abm7285.

37. Raulin, A.C., Kraft, L., Al-Hilaly, Y.K., Xue, W.F., McGeehan, J.E., Atack, J.R., and Serpell, L. (2019). The molecular basis for apolipoprotein E4 as the major risk factor for late-onset Alzheimer's disease. J. Mol. Biol. *431*, 2248–2265. https://doi.org/10.1016/j.jmb.2019.04.019.

38. Hatters, D.M., Zhong, N., Rutenber, E., and Weisgraber, K.H. (2006). Amino-terminal domain stability mediates apolipoprotein E aggregation into neurotoxic fibrils. J. Mol. Biol. *361*, 932–944. https://doi.org/10.1016/j.jmb.2006.06.080.

39. Friesen, M., and Meyer-Luehmann, M. (2019). Abeta seeding as a tool to study cerebral amyloidosis and associated pathology. Front. Mol. Neurosci. *12*, 233. https://doi.org/10.3389/fnmol.2019.00233.

40. Ruiz-Riquelme, A., Lau, H.H.C., Stuart, E., Goczi, A.N., Wang, Z., Schmitt-Ulms, G., and Watts, J.C. (2018). Prion-like propagation of beta-amyloid aggregates in the absence of APP overexpression. Acta Neuropathol. Commun. *6*, 26. https://doi.org/10.1186/s40478-018-0529-x.

41. Meyer-Luehmann, M., Coomaraswamy, J., Bolmont, T., Kaeser, S., Schaefer, C., Kilger, E., Neuenschwander, A., Abramowski, D., Frey, P., Jaton, A.L., et al. (2006). Exogenous induction of cerebral beta-amyloidogenesis is governed by agent and host. Science *313*, 1781–1784. https://doi.org/10.1126/science.1131864.

42. Filipello, F., You, S.F., Mirfakhar, F.S., Mahali, S., Bollman, B., Acquarone, M., Korvatska, O., Marsh, J.A., Sivaraman, A., Martinez, R., et al. (2023). Defects in lysosomal function and lipid metabolism in human microglia harboring a TREM2 loss of function mutation. Acta Neuropathol. *145*, 749–772. https://doi.org/10.1007/s00401-023-02568-y.

43. Wang, Y., Cella, M., Mallinson, K., Ulrich, J.D., Young, K.L., Robinette, M.L., Gilfillan, S., Krishnan, G.M., Sudhakar, S., Zinselmeyer, B.H., et al. (2015). TREM2 lipid sensing sustains the microglial response in an Alzheimer's disease model. Cell *160*, 1061–1071. https://doi.org/10.1016/j.cell.2015.01.049.

44. Goldstein, J.L., Brown, M.S., Anderson, R.G., Russell, D.W., and Schneider, W.J. (1985). Receptor-mediated endocytosis: concepts emerging from the LDL receptor system. Annu. Rev. Cell Biol. *1*, 1–39. https://doi.org/10.1146/annurev.cb.01.110185.000245.

45. Prinz, M., Jung, S., and Priller, J. (2019). Microglia biology: one century of evolving concepts. Cell *179*, 292–311. https://doi.org/10.1016/j.cell.2019.08.053.

46. Hansen, D.V., Hanson, J.E., and Sheng, M. (2018). Microglia in Alzheimer's disease. J. Cell Biol. *217*, 459–472. https://doi.org/10.1083/jcb.201709069.

47. Heneka, M.T., Carson, M.J., El Khoury, J., Landreth, G.E., Brosseron, F., Feinstein, D.L., Jacobs, A.H., Wyss-Coray, T., Vitorica, J., Ransohoff, R.M., et al. (2015). Neuroinflammation in Alzheimer's disease. Lancet Neurol. *14*, 388–405. https://doi.org/10.1016/S1474-4422(15)70016-5.

48. Lewcock, J.W., Schlepckow, K., Di Paolo, G., Tahirovic, S., Monroe, K.M., and Haass, C. (2020). Emerging microglia biology defines novel therapeutic approaches for Alzheimer's disease. Neuron *108*, 801–821. https://doi.org/10.1016/j.neuron.2020.09.029.

49. Ulrich, J.D., Ulland, T.K., Colonna, M., and Holtzman, D.M. (2017). Elucidating the role of TREM2 in Alzheimer's disease. Neuron *94*, 237–248. https://doi.org/10.1016/j.neuron.2017.02.042.

50. Spangenberg, E.E., Lee, R.J., Najafi, A.R., Rice, R.A., Elmore, M.R.P., Blurton-Jones, M., West, B.L., and Green, K.N. (2016). Eliminating microglia in Alzheimer's mice prevents neuronal loss without modulating amyloid-beta pathology. Brain *139*, 1265–1281. https://doi.org/10.1093/brain/aww016.

51. Grathwohl, S.A., Kälin, R.E., Bolmont, T., Prokop, S., Winkelmann, G., Kaeser, S.A., Odenthal, J., Radde, R., Eldh, T., Gandy, S., et al. (2009). Formation and maintenance of Alzheimer's disease beta-amyloid plaques in the absence of microglia. Nat. Neurosci. *12*, 1361–1363. https://doi.org/10.1038/nn.2432.

52. Kiani Shabestari, S., Morabito, S., Danhash, E.P., McQuade, A., Sanchez, J.R., Miyoshi, E., Chadarevian, J.P., Claes, C., Coburn, M.A., Hasselmann, J., et al. (2022). Absence of microglia promotes diverse pathologies and early lethality in Alzheimer's disease mice. Cell Rep. *39*, 110961. https://doi.org/10.1016/j.celrep.2022.110961.

53. Spangenberg, E., Severson, P.L., Hohsfield, L.A., Crapser, J., Zhang, J., Burton, E.A., Zhang, Y., Spevak, W., Lin, J., Phan, N.Y., et al. (2019). Sustained microglial depletion with CSF1R inhibitor impairs parenchymal plaque development in an Alzheimer's disease model. Nat. Commun. *10*, 3758. https://doi.org/10.1038/s41467-019-11674-z.

54. Huang, Y., Happonen, K.E., Burrola, P.G., O'Connor, C., Hah, N., Huang, L., Nimmerjahn, A., and Lemke, G. (2021). Microglia use TAM receptors to detect and engulf amyloid beta plaques. Nat. Immunol. *22*, 586–594. https://doi.org/10.1038/s41590-021-00913-5.

55. Liu, C.C., Zhao, N., Fu, Y., Wang, N., Linares, C., Tsai, C.W., and Bu, G. (2017). ApoE4 accelerates early seeding of amyloid pathology. Neuron *96*, 1024–1032.e3. https://doi.org/10.1016/j.neuron.2017.11.013.

56. Hashimoto, T., Serrano-Pozo, A., Hori, Y., Adams, K.W., Takeda, S., Banerji, A.O., Mitani, A., Joyner, D., Thyssen, D.H., Bacskai, B.J., et al. (2012). Apolipoprotein E, especially apolipoprotein E4, increases the oligomerization of amyloid beta peptide. J. Neurosci. *32*, 15181–15192. https://doi.org/10.1523/JNEUROSCI.1542-12.2012.

57. Castano, E.M., Prelli, F., Wisniewski, T., Golabek, A., Kumar, R.A., Soto, C., and Frangione, B. (1995). Fibrillogenesis in Alzheimer's disease of amyloid beta peptides and apolipoprotein E. Biochem. J. *306*, 599–604. https://doi.org/10.1042/bj3060599.

58. Chan, W., Fornwald, J., Brawner, M., and Wetzel, R. (1996). Native complex formation between apolipoprotein E isoforms and the Alzheimer's disease peptide A beta. Biochemistry *35*, 7123–7130. https://doi.org/10.1021/bi952852v.

59. Wagner, J., Degenhardt, K., Veit, M., Louros, N., Konstantoulea, K., Skodras, A., Wild, K., Liu, P., Obermüller, U., Bansal, V., et al. (2022). Medin co-aggregates with vascular amyloid-beta in Alzheimer's disease. Nature *612*, 123–131. https://doi.org/10.1038/s41586-022-05440-3.

60. Irwin, D.J., Lee, V.M.Y., and Trojanowski, J.Q. (2013). Parkinson's disease dementia: convergence of alpha-synuclein, tau and amyloid-beta pathologies. Nat. Rev. Neurosci. *14*, 626–636. https://doi.org/10.1038/nrn3549.

61. Parhizkar, S., Arzberger, T., Brendel, M., Kleinberger, G., Deussing, M., Focke, C., Nuscher, B., Xiong, M., Ghasemigharagoz, A., Katzmarski, N., et al. (2019). Loss of TREM2 function increases amyloid seeding but reduces plaque-associated ApoE. Nat. Neurosci. *22*, 191–204. https://doi.org/10.1038/s41593-018-0296-9.

62. d'Errico, P., Ziegler-Waldkirch, S., Aires, V., Hoffmann, P., Mezö, C., Erny, D., Monasor, L.S., Liebscher, S., Ravi, V.M., Joseph, K., et al. (2022). Microglia contribute to the propagation of Abeta into unaffected brain tissue. Nat. Neurosci. *25*, 20–25. https://doi.org/10.1038/s41593-021-00951-0.

63. Roy, E.R., Wang, B., Wan, Y.W., Chiu, G., Cole, A., Yin, Z., Propson, N.E., Xu, Y., Jankowsky, J.L., Liu, Z., et al. (2020). Type I interferon response drives neuroinflammation and synapse loss in Alzheimer disease. J. Clin. Invest. *130*, 1912–1930. https://doi.org/10.1172/JCI133737.

64. Hammond, T.R., Dufort, C., Dissing-Olesen, L., Giera, S., Young, A., Wysoker, A., Walker, A.J., Gergits, F., Segel, M., Nemesh, J., et al. (2019). Single-cell RNA sequencing of microglia throughout the mouse lifespan and in the injured brain reveals complex cell-state changes. Immunity *50*, 253–271.e6. https://doi.org/10.1016/j.immuni.2018.11.004.

65. Deczkowska, A., Matcovitch-Natan, O., Tsitsou-Kampeli, A., Ben-Hamo, S., Dvir-Szternfeld, R., Spinrad, A., Singer, O., David, E., Winter, D.R., Smith, L.K., et al. (2017). Mef2C restrains microglial inflammatory response and is lost in brain ageing in an IFN-I-dependent manner. Nat. Commun. *8*, 717. https://doi.org/10.1038/s41467-017-00769-0.

66. Mathys, H., Adaikkan, C., Gao, F., Young, J.Z., Manet, E., Hemberg, M., De Jager, P.L., Ransohoff, R.M., Regev, A., and Tsai, L.H. (2017). Temporal tracking of microglia activation in neurodegeneration at single-cell resolution. Cell Rep. *21*, 366–380. https://doi.org/10.1016/j.celrep.2017.09.039.

67. Zhang, H., Zoued, A., Liu, X., Sit, B., and Waldor, M.K. (2020). Type I interferon remodels lysosome function and modifies intestinal epithelial defense. Proc. Natl. Acad. Sci. USA *117*, 29862–29871. https://doi.org/10.1073/pnas.2010723117.

68. Millet, A., Ledo, J.H., and Tavazoie, S.F. (2024). An exhausted-like microglial population accumulates in aged and APOE4 genotype Alzheimer's brains. Immunity *57*, 153–170.e6. https://doi.org/10.1016/j.immuni.2023.12.001.

69. Saito, T., Matsuba, Y., Mihira, N., Takano, J., Nilsson, P., Itohara, S., Iwata, N., and Saido, T.C. (2014). Single App knock-in mouse models of Alzheimer's disease. Nat. Neurosci. *17*, 661–663. https://doi.org/10.1038/nn.3697.

70. Schindelin, J., Arganda-Carreras, I., Frise, E., Kaynig, V., Longair, M., Pietzsch, T., Preibisch, S., Rueden, C., Saalfeld, S., Schmid, B., et al. (2012). Fiji: an open-source platform for biological-image analysis. Nat. Methods *9*, 676–682. https://doi.org/10.1038/nmeth.2019.

71. Concordet, J.P., and Haeussler, M. (2018). CRISPOR: intuitive guide selection for CRISPR/Cas9 genome editing experiments and screens. Nucleic Acids Res. *46*, W242–W245. https://doi.org/10.1093/nar/gky354.

72. Su, B., Bettcher, L.F., Hsieh, W.Y., Hornburg, D., Pearson, M.J., Blomberg, N., Giera, M., Snyder, M.P., Raftery, D., Bensinger, S.J., et al. (2021). A DMS shotgun lipidomics workflow application to facilitate high-throughput, comprehensive lipidomics. J. Am. Soc. Mass Spectrom. *32*, 2655–2663. https://doi.org/10.1021/jasms.1c00203.

73. Abud, E.M., Ramirez, R.N., Martinez, E.S., Healy, L.M., Nguyen, C.H.H., Newman, S.A., Yeromin, A.V., Scarfone, V.M., Marsh, S.E., Fimbres, C., et al. (2017). iPSC-derived human microglia-like cells to study neurological diseases. Neuron *94*, 278–293.e9. https://doi.org/10.1016/j.neuron.2017.03.042.

74. Kaji, S., Maki, T., Kinoshita, H., Uemura, N., Ayaki, T., Kawamoto, Y., Furuta, T., Urushitani, M., Hasegawa, M., Kinoshita, Y., et al. (2018). Pathological endogenous alpha-synuclein accumulation in oligodendrocyte precursor cells potentially induces inclusions in multiple system atrophy. Stem Cell Rep. *10*, 356–365. https://doi.org/10.1016/j.stemcr.2017.12.001.

75. Shirotani, K., Tomioka, M., Kremmer, E., Haass, C., and Steiner, H. (2007). Pathological activity of familial Alzheimer's disease-associated mutant presenilin can be executed by six different gamma-secretase complexes. Neurobiol. Dis. *27*, 102–107. https://doi.org/10.1016/j.nbd.2007.04.011.

76. Tarutani, A., Arai, T., Murayama, S., Hisanaga, S.I., and Hasegawa, M. (2018). Potent prion-like behaviors of pathogenic alpha-synuclein and evaluation of inactivation methods. Acta Neuropathol. Commun. *6*, 29. https://doi.org/10.1186/s40478-018-0532-2.

77. Ziegler-Waldkirch, S., d'Errico, P., Sauer, J.F., Erny, D., Savanthrapadian, S., Loreth, D., Katzmarski, N., Blank, T., Bartos, M., Prinz, M., et al. (2018). Seed-induced Abeta deposition is modulated by microglia under environmental enrichment in a mouse model of Alzheimer's disease. EMBO J. *37*, 167–182. https://doi.org/10.15252/embj.201797021.

78. Berghoff, S.A., Spieth, L., Sun, T., Hosang, L., Schlaphoff, L., Depp, C., Düking, T., Winchenbach, J., Neuber, J., Ewers, D., et al. (2021). Microglia facilitate repair of demyelinated lesions via post-squalene sterol synthesis. Nat. Neurosci. *24*, 47–60. https://doi.org/10.1038/s41593-020-00757-6.

79. Hubin, E., Verghese, P.B., van Nuland, N., and Broersen, K. (2019). Apolipoprotein E associated with reconstituted high-density lipoprotein-like particles is protected from aggregation. FEBS Lett. *593*, 1144–1153. https://doi.org/10.1002/1873-3468.13428.

80. Yeh, F.L., Wang, Y., Tom, I., Gonzalez, L.C., and Sheng, M. (2016). TREM2 binds to apolipoproteins, including APOE and CLU/APOJ, and thereby facilitates uptake of amyloid-beta by microglia. Neuron *91*, 328–340. https://doi.org/10.1016/j.neuron.2016.06.015.

81. Kislinger, G., Gnägi, H., Kerschensteiner, M., Simons, M., Misgeld, T., and Schifferer, M. (2020). Multiscale ATUM-FIB microscopy enables targeted ultrastructural analysis at isotropic resolution. iScience *23*, 101290. https://doi.org/10.1016/j.isci.2020.101290.

Please cite this article in press as: Kaji et al., Apolipoprotein E aggregation in microglia initiates Alzheimer's disease pathology by seeding β-amyloidosis, Immunity (2024), https://doi.org/10.1016/j.immuni.2024.09.014

STAR★METHODS

KEY RESOURCES TABLE

REAGENT or RESOURCE	SOURCE	IDENTIFIER
Antibodies		
Aβ1-11	Biolegend	Cat #835104; RRID:AB_2632642
Aβ 2D8	Dr. Michael Willem	N/A
Aβ 6E10	Biolegend	Cat #803001; RRID:AB_2564653
Aβ 6E10 biotinylated	Biolegend	Cat #803007; RRID:AB_2564657
Aβ D3E10	Cell signaling	Cat #12843S; RRID:AB_2798041
Aldh1l1	Sigma	Cat #45-WH0010840M1; RRID:AB_1839537
APP	Abcam	Cat #ab32136; RRID:AB_2289606
ApoE 8D4	Dr. Michael Willem	N/A
ApoE	Abcam	Cat #ab52607; RRID:AB_867704
ApoE biotinylated	Novus	Cat #NBP1-31123B; RRID:AB_3206554
AT8	Thermofisher	Cat #MN1020; RRID:AB_223647
β-actin	Sigma	Cat #A2228; RRID:AB_476697
Bcas1	Novus Biologicals	Cat #NBP2-38736; RRID:AB_3298159
CD68	Bio-Rad	Cat #MCA1957; RRID:AB_322219
Ferritin Heavy Chain	Abcam	Cat #ab65080; RRID:AB_10564857
Gfap	Synaptic Systems	Cat #173004; RRID:AB_10641162
Halo-Tag	Promega	Cat #G9281; RRID:AB_713650
Iba1	Synaptic Systems	Cat #234006; RRID:AB_2619949
Iba1	FujiFilm Wako	Cat #019-19741; RRID:AB_839504
NeuN	Millipore	Cat #ABN91; RRID:AB_11205760
Lamp1	Santa Cruz	Cat #Sc-19992; RRID:AB_2134495
Pdgfra	R&D Systems	Cat #AF1062; RRID:AB_2236897
Plin2	Bio-techne	Cat #NB110-40877; RRID:AB_787904
Stat1	CST	Cat #14994S; RRID:AB_2737027
Streptavidin (HRP)	Abcam	Cat #ab7403
Alexa488 d α-chicken	Jackson	Cat #703-545-155; RRID:AB_2340375
Alexa488 d α-guinea pig	Sigma	Cat #SAB4600298
Alexa488 d α-rat	Invitrogen	Cat #A21208; RRID:AB_2535794
Alexa555 d α-rat	Thermo	Cat #A48270; RRID:AB_2896336
Alexa647 g α-rat	Thermo	Cat #A21235; RRID:AB_2535804
Alexa647 d α-rabbit	Thermo	Cat #A31573; RRID:AB_2536183
Alexa647 d α-rat	Jackson	Cat #712-605-150; RRID:AB_2340693
g α-rat IgG HRP	Thermo	Cat #62-9520; RRID:AB_2533965
g α-mouse IgG HRP	Thermo	Cat #31430; RRID:AB_228307
g α-chicken IgG HRP	Invitrogen	Cat #A16054; RRID:AB_2534727
g α-rabbit 10 nm gold	Aurion	Cat #810.011
Biological samples		
Human cortical brain blocks	See Table S1	N/A
Chemicals, peptides, and recombinant proteins		
Congo Red	Sigma	Cat #C6767
Draq5	Life	Cat #62251
Hoechst	Thermo	Cat #H3570
NucRed	Invitrogen	Cat #R37113
Methoxy-XO4	Tocris	Cat #4920

(*Continued on next page*)

Please cite this article in press as: Kaji et al., Apolipoprotein E aggregation in microglia initiates Alzheimer's disease pathology by seeding β-amyloidosis, Immunity (2024), https://doi.org/10.1016/j.immuni.2024.09.014

Continued

REAGENT or RESOURCE	SOURCE	IDENTIFIER
Opal dye 520	Perkin Elmer	Cat #FP1487001
Opal dye 570	Perkin Elmer	Cat #FP1488001
Opal dye 620	Perkin Elmer	Cat #FP1495001
Phalloidin	Abcam	Cat #ab176753
ThiazineRed	Morphisto	Cat #12990.00100
Thioflavin-S	Sigma	Cat #T1893
Thioflavin T	Sigma	Cat #T3516
TMR Halo ligand	Promega	Cat #G8251
HaloTag® Fluorescent Ligand R110Direct	Promega	Cat #G322A
Beta-amyloid (1-42)	AnaSpec	Cat #AS-64129-1
Beta-Amyloid (1-42), HiLyte Fluor 488-labeled	AnaSpec	Cat #AS-60479-01
APOE3, human	produced by BiologicsCorp	N/A
APOE4, human	produced by BiologicsCorp	N/A
APOE, mouse	produced by BiologicsCorp	N/A
APOE-Halo, mouse	produced by BiologicsCorp	N/A
Bafilomycin	InvivoGen	Cat #tlrl-baf1
Baricitinib	InvivoChem	Cat #V0338
Chloroquine	Sigma	Cat #C6628
Cholesterol	Sigma	Cat #C8667
cOmplete™, EDTA-free Protease Inhibitor Cocktail	Roche	Cat #11873580001
Diethylamine	Sigma	Cat #471216
EDTA (0.5 M), pH 8.0, RNase-free	Invitrogen	Cat #AM9261
Guanidine hydrochloride	Sigma	Cat #G3272
Imperial Protein Stain	ThermoFisher	Cat #24615
Interferon-γ protein	Merck	Cat #IF005
4x Laemmli Sample Buffer	BioRad	Cat #1610747
Leupeptin	ThermoFisher	Cat #78435
Lipopolysaccharide	Sigma	Cat #L4391
Lys05	Selleckchem	Cat #S8369
N-Lauroylsarcosine sodium salt	Sigma	Cat #61745
OptiPrep™ Density Gradient Medium	Sigma	Cat #D1556
16:0-18:1 PC (POPC)	Avanti polar lipids	Cat #850457
Pierce™ ECL Western Blotting-Substrat	ThermoFisher	Cat #32106
PLX5622	MedChemExpress	Cat #HY-114153
Ready Blue® Protein Gel Stain	Sigma	Cat #RSB
SDS ultra pure	Roth	Cat #155626
SeeBlue™ Plus2 vorgefärbter Proteinstandard	Invitrogen	Cat #LC5925
Sodium cholate hydrate	Sigma	Cat #C9282
Sodium deoxycholate	Sigma	Cat #D6750
TopFluor TMR cholesterol	Avanti polar lipids	Cat #810385
Tricine, ultra pure	biomol	Cat #22870
Triton™ X-100	Sigma	Cat #T8787
Critical commercial assays		
Adult brain dissociation kit	Miltenyi biotec	Cat #130-107-677
BC assay protein kit	Interchim	Cat #FT-40840A
ChromoTek Halo-Trap Magnetic Agarose Kit	Proteintech	Cat #otma
CRISPRevolution sgRNA EZ Kit	Synthego	Purchased with Guides

(*Continued on next page*)

Please cite this article in press as: Kaji et al., Apolipoprotein E aggregation in microglia initiates Alzheimer's disease pathology by seeding β-amyloidosis, Immunity (2024), https://doi.org/10.1016/j.immuni.2024.09.014

Continued

REAGENT or RESOURCE	SOURCE	IDENTIFIER
DynabeadsTM M-280 Streptavidin	ThermoFisher	Cat #11205D
Fujifilm Medical X-ray Film Super RX-N	Fujifilm	Cat #47410
GoTaq qPCR master mix	Promega	Cat #A6001
Neuronal tissue dissociation kit	Miltenyi biotec	Cat #130-092-628
Novex™ Tris-Glycine Mini Protein Gels, 4–12%, 1.0 mm, WedgeWell™	Invitrogen	Cat #XP04122BOX
Novex™ 10 to 20%, Tricine, 1.0 mm, Mini Protein Gels	Invitrogen	Cat #EC6625BOX, EC66252BOX, EC66255BOX
Novex™ Tris-Glycin Nativer Probenpuffer (2x)	Invitrogen	Cat #LC2673
Ovation PicoSL WTA system v2 protocol	NuGEN	Cat #3403-60
Powerup Sybr Green master mix	Applied biosystems	Cat #A25741
P3 Primary Cell 4D-Nucleofector™ X Kit S	Lonza	Cat #V4XP-3032
RNeasy MikroKit	Qiagen	Cat #74104
STEMdiff Hematopoietic Kit	Stem Cell Tecnologies	Cat #05310
Superscript III	Invitrogen	Cat #18080093
XCell SureLock™ Mini-Cell und XCell II™ Blot Modul	Invitrogen	Cat #EI0001
Experimental models: Cell lines		
Mouse: BV-2 macrophages	Accegen	Cat #ABC-TC212S
Mouse: BV-2 FDFT1 KO	In this paper	N/A
Mouse: BV-2 TREM2 KO	In this paper	N/A
Human: Female episomal iPSC line A18944	ThermoFisher	Cat #A18945
Experimental models: mouse lines		
C57BL/6J	The Jackson Laboratory	Strain #000664 MGI:3028467
Mouse: B6.Cg-Tg(APPSwFlLon,PSEN1*M146L*L286V)6799Vas/Mmjax	The Jackson Laboratory	Strain #034840
Mouse: B6.129P2-Apoetm1Unc/J	The Jackson Laboratory	Strain #002052 MGI:2163789
Mouse: B6.129P2-Apoetm1Unc/J (APPSwFlLon,PSEN1*M146L*L286V)6799Vas	In this paper	N/A
Mouse: B6.Cg-Apoe<em2(APOE*)Adiuj>/J x B6.Cg-Tg(APPSwFlLon,PSEN1*M146L*L286V)6799Vas/Mmjax	In this paper	N/A
Mouse: B6(SJL)-Apoe<tm1.1(APOE*4)Adiuj>/J x B6.Cg-Tg(APPSwFlLon,PSEN1*M146L*L286V)6799Vas/Mmjax	In this paper	N/A
Mouse: B6J-Apoe<em2(HaloTag7)Bwef>	In this paper	N/A
Mouse: B6J-Apoe<em2(HaloTag7)Bwef> Tg(APPSwFlLon,PSEN1*M146L*L286V)6799Vas	In this paper	N/A
Mouse: Tg(Thy1-APPSw,Thy1-PSEN1*L166P)21JckrMouse:	The Jackson Laboratory	Strain #037891 MGI:3765455
Mouse: B6.129P2-TREM2tm1cln/ Tg(Thy1-APPSw,Thy1-PSEN1*L166P)21Jckr	In this paper	N/A
Mouse: APP<tm3.1Tcs>	Saito et al.[69]	MGI:5637817
Mouse: B6.129P2(C)-Cx3cr1tm2.1(cre/ERT2)Jung/J Tg(APPSwFlLon,PSEN1*M146L*L286V)6799Vas	In this paper	N/A

(*Continued on next page*)

Continued

REAGENT or RESOURCE	SOURCE	IDENTIFIER
Mouse: FDFT1 fl/fl B6.129P2(C)-Cx3cr1tm2.1(cre/ERT2)Jung/J Tg(APPSwFlLon,PSEN1*M146L*L286V) 6799Vas	In this paper	N/A
Mouse: B6.129S(Cg)-Stat1tm1Dlv/J Tg(APPSwFlLon,PSEN1*M146L*L286V) 6799Vas/Mmjax	In this paper	N/A
Oligonucleotides		
qPCR/genotyping PCR primers	See Table S2	N/A
Software and algoritms		
Arivis Vision4D v3.2	Zeiss	https://www.zeiss.de
Biorender	Biorender	https://www.biorender.com
Image J (Fiji)	Schindelin et al.[70]	https://imagej.net/Fiji
GraphPad Prism 9	GraphPad Software, Inc.	https://www.graphpad.com/
Imaris	Oxford instruments	Imaris 10
QuPath-0.3.2	GitHub	https://doi.org/10.1038/s41598-017-17204-5
ZEN 3.2 blue edition	Zeiss	https://www.zeiss.de

EXPERIMENTAL MODEL AND STUDY PARTICIPANT DETAILS

Human autopsy samples

Human AD patient material was obtained from the Neurobank Munich and experiments were performed with full ethical consent from the ethics committee at the LMU Munich (see Table S1 for patient demographic data).

Cell lines and primary cells

Both cell lines and primary cells were cultured in a humidified incubator (5% CO2, 37°C) until use. Primary mouse microglia, astrocytes, and mixed glial cells were established from 2–15 days old *C57BL/6J* mice (mixed gender). Generation of *FDFT1* and *TREM2 KO* BV2 is described in method details.

Mice

All experiments were performed in accordance with the German animal welfare law and local regulations for animal experiments of Bavaria and Lower-Saxony. Animals were group housed (3–5 mice) in a controlled environment (temperature of 22°C, 30–70% humidity, 12 h dark/12 h light cycle) and had access to food and water ad libitum under specific pathogen free conditions. Male and female *C57BL/6J* mice (Age > 6 weeks if not state otherwise) or genetic mouse mutants (Age > 6 weeks if not state otherwise) were taken for all experiments. Animals of the same sex and age were randomly assigned to experimental groups (3–6 mice per group). Mice from different genotypes were cohoused. Mice did not undergo any procedures prior to the described experiments. Mice used in this study include *C57BL/6J*, *ApoE KO*, *ApoE-Halo, 5xFAD*, *5xFAD ApoE-Halo*, *5xFAD ApoE KO*, *APP-NL-G-F*, *APP/PS1*, *APP/PS1 Trem2-KO*, *STAT1 KO 5xFAD, 5xFAD CR3CR1Cre-YFP*, *5xFAD FDFT1 KO* mice.

METHOD DETAILS

Mice

C57BL/6J, *5xFAD*, *ApoE KO*, *Cx3Cr1-CreERT2* mice were purchased from Charles River Laboratories. *APOE3 KI, APOE4 KI, Stat1 KO* mice were purchased from Jackson Laboratory. Tissue sections from *APP-NL-G-F, APP/PS1* and *APP/PS1 Trem2-KO* were kindly provided by Christian Haass. Generation of *ApoE-Halo* mice is described below. *5xFAD* mice were crossbred to *ApoE KO* to generate *5xFAD ApoE KO* mice (paternal *5xFAD* transgene delivery). *5xFAD ApoE-Halo* mice were generated by cross-breeding *5xFAD* mice with *ApoE-Halo* mice (paternal *5xFAD* transgene delivery). *APOE3 KI* or *APOE4 KI* mice were crossbred with *5xFAD* mice (paternal *5xFAD* transgene delivery) to generate *5xFAD APOE3 KI* and *5xFAD APOE4 KI* mice (paternal *5xFAD* transgene delivery). *STAT1 KO* mice were crossbred with *5xFAD* mice to generate *STAT1 KO 5xFAD* mice (paternal *5xFAD* transgene delivery). Conditional cholesterol synthesis mutants were generated by cross-breeding *Cx3Cr1-CreERT2* mice with mice harboring *SQS/FDFT1* with two *loxP* sites flanking exon 5, referred to as *FDFT1 KO* (*CX3CR1 CreERT2*$^{+/-}$ *FDFT1*$^{flox/flox}$). Conditional microglial cholesterol synthesis mutants were crossbred with *5xFAD mice* Random 5xFAD transgene delivery) to generate *FDFT1 KO 5xFAD mice* (*CX3CR1CreERT*$^{+/-}$ *FDFT1*$^{flox/flox}$ *5xFAD*$^{+/-}$). *FDFT1 KO 5xFAD* mice were compared to the respective controls (*Cx3Cr1Cre*

5xFAD; *CX3CR1CreERT2*$^{+/-}$ *5xFAD*$^{+/-}$). Conditional mouse mutants and respective controls received tamoxifen dissolved in corn oil by intraperitoneal injections in five consecutive days at a concentration of 75 μg/g of body weight to induce recombination.

Generation of APOE-Halo reporter mice

APOE-Halo reporter mice were generated by CRISPR/Cas9-assisted gene editing in mouse zygotes. Briefly, pronuclear stage zygotes were obtained by mating *C57BL/6J* males with superovulated *C57BL/6J* females (Charles River). Embryos were then microinjected into the male pronucleus with an *ApoE*-specific CRISPR/Cas9 ribonucleoprotein (RNP) solution consisting of 30 ng/μl SpCas9 HiFi protein (IDT), 0.6 μM crRNA (IDT), 0.6 μM tracrRNA (IDT), and 5 ng/μl of a mutagenic targeting vector for the introduction of a HaloTag linker and the HaloTag7 coding sequence (Promega) right before the *ApoE* stop codon. The lengths of the homology arms were 900 and 1000 bp, respectively. After microinjection, treated zygotes were transferred into pseudopregnant CD-1 foster animals. Mutant founder animals were crossed to *C57BL/6J* animals to isolate the respective allele. Validation of the targeted loci was performed on genomic DNA from F1 animals by RFLP, Sanger sequencing, and qPCR-based copy number assays. To exclude additional unwanted modifications, putative off-target sites of the *ApoE*-specific crRNA were predicted using the CRISPOR online tool.[71] Predicted loci were PCR-amplified and verified by Sanger sequencing. Validated animals without any off-target mutations were used for further breeding. All animal were housed in standard cages in a specific pathogen-free facility on a 12 h light/dark cycle with ad libitum access to food and water.

Treatments to mice

Mice were fed normal chow (ssniff V1124), if not specified. For the cohort of microglial depletion, 5xFAD and *5xFAD ApoE KO* mice were fed either Control AIN-76A standard chow or 0.12% PLX5622 (MedChemExpress, formulated in AIN-76A standard chow by Research Diets Inc.). Treatments were started at the age of 7 weeks provided ad libitum and continued until the age of 11–12 weeks. For the cohort of Baricitinib treatment, *5xFAD* mice were fed powdered chow (ssniff V1120) or powdered chow supplemented with Baricitinib (InvivoChem, V0338,) 10 mg/kg body weight solved in corn oil. Treatments were started at the age of 6 weeks provided ad libitum. For the chloroquine treatment, *5xFAD* mice were injected intraperitoneally every day with 45 mg/kg bodyweight (Sigma) while control mice were injected with the same amount of saline. Treatments were started at the age of 11 weeks for 7days.

Serum analysis

Animals were anesthetized by intraperitoneal injection of Avertin (tribromethanol), serum was prepared by 4 h clotting and centrifugation of blood from cardiac puncture. Cholesterol determination measurement of LDL- and HDL -cholesterol, as well as triglycerides were assessed with the Architect II system from Abbott Diagnostics. Fast protein liquid chromatography (FPLC) analysis of serum was performed with Superdex^{TM} 200 Increase 10/300GL column equilibrated in 10 mM Tris pH 7.5, 150 mM NaCl, 1 mM EDTA buffer.

Cholesterol ester analysis by mass spectrometry

The analysis followed standardized, quantitative protocols.[72] Briefly, 25 μL of plasma was spiked with deuterated internal standards followed by a methyl tert-butyl ether-based extraction protocol. In case of brain tissue, samples were homogenized in a bullet blender (Next Avance) and aliquots corresponding to 5 mg tissue were processed accordingly. After drying under a gentle stream of nitrogen, samples were taken up in running buffer (methanol:dichloromethane 1:1, containing 10 mM ammonium acetate) and injected into a differential mobility spectroscopy (DMS) based flow-injection shotgun lipidomics platform, consisting of a SCIEX QTRAP 5500 mass spectrometer equipped with SelexION DMS interface and a Nexera X2 UHPLC-system. Shotgun Lipiomics Assistant software was used to process data files and report the lipid concentration.[72]

Isolation of serum and brain APOE-Halo from *ApoE-Halo* mice for EM analysis

Isolation of APOE-Halo positive lipoparticles from serum and brain lysate was performed by immunoprecipitation using the ChromoTek Halo-Trap Magnetic Agarose Kit (Proteintech) according to manufacturer's instruction. Serum from *ApoE-Halo* animals was collected as described above, and 200 μl of serum was used as the input material for immunoprecipitation. For the preparation of brain-derived HDL-like lipoparticles, brain tissue was homogenized with RIPA buffer (10 mM Tris pH 7.5, 150 mM NaCl, 0.5 mM EDTA, 0.1% SDS, 1% Triton™ X-100, 1% deoxycholate) followed by centrifuge at 17,000 g for 10 min at 4°C. The supernatant was subjected to a density gradient using OptiPrep™ Density Gradient Medium (Sigma) to separate the HDL-like lipoparticles. The fraction corresponding to the density of 1.146-1.204 g/ml was collected as a lipoparticle fraction after the ultracentrifugation at 54.000 g for 3 h at 4°C, and 200 μl of purified lipoparticles was used as the input material for immunoprecipitation. Each sample was analyzed by EM immediately after the isolation.

Isolation of MX04^{+} microglia in *5xFAD* mice

Microglia were isolated by magnetic cell isolation (MACS) according to the adult brain dissociation protocol or the neuronal tissue dissociation protocol (Miltenyi biotec), respectively of the age of animals. For analysis of seed containing microglia, mechanically dissociated tissue was stained with 0.4 mg/ml Methoxy-X04 (MX04, Tocris) for 30 min at 37°C prior to enzymatic dissociation. Antibody labeling was done according to the CD11b Microbead protocol and isolated by positive selection. For fluorescence-activated cell sorting (FACS) analysis, cells were transferred in HBSS buffer including 10 mM HEPES. Isolated CD11b positive microglia were sorted for YFP (CX3CR1 CreERT2 harboring a YFP reporter) and MX04 positivity using a FACSAria 4L SORP cell sorter (Becton

Dickinson) operated by FACS Diva software (Becton Dickinson). Small debris was removed with preliminary gating of FSC/SSC. Doublet exclusion enabled an analysis of single cells. Analyzed cells were defined by endogenous YFP expression and populations distinguished by the fluorescent staining of MX04. Isolated cell populations were collected and centrifuged for lysing in RLT buffer (Qiagen) for further expression analysis. Cell quantification was performed using a CytoFLEX (Beckman Coulter) operated by CytExpert software (Beckman Coulter, v2.4) and allowed by the additional usage of CaliBRITE APC beads (BD).

mRNA expression analysis

For expression analysis of cell lysate, RNA was extracted using RNeasy MikroKit (Qiagen). RNA concentration and quality of cell culture samples were determined using NanoDrop spectrometer, and cDNA was synthesized with Superscript III (Invitrogen). Sorted cell populations were further processed for RNA/cDNA amplification according to Ovation PicoSL WTA system v2 protocol (NuGEN). Quantitative PCRs were done in triplicates using the GoTaq qPCR master mix (Promega) or Powerup Sybr Green master mix (Applied biosystems) and the LightCycler 480 (Roche Diagnostics). Measured Ct values were normalized to the mean of housekeeping genes (*18S, Hprt, Rps13, Rplp0*). Quantification was done by applying the ΔΔCt method, normalized to experimental controls. All primers were designed to fulfill optimal criteria e.g. length, melting temperature, GC content, low number of repeats, and amplicon length. All primers were intron-spanning. For primer sequences see Key Resources.

Sterol measurements

Sterol abundance was quantified by lipid GC-MS or GC-MS/MS in human CSF, APOE isolated from human CSF and acutely isolated CD11b positive cells from 6-month-old wildtype and *5xFAD* mice. Samples were lyophilized at a shelf temperature of –56°C for 24 h under vacuum of 0.2 millibars (Christ LMC-1 BETA 1-16). Metabolites were extracted in a two-phase system of 3:1 methyl-tert-butyl ether:methanol (vol/vol) and water, and pentadecanoic acid was added as an internal standard. The organic phase (10–200 μl) was dried under a stream of nitrogen, dissolved in 10–15 μl pyridine and derivatized with twice the volume of N-methyl-N-(trimethylsilyl) trifluoroacetamide (MSTFA) to transform the sterols and the standard to their trimethylsilyl (TMS) derivatives. Each sample was analyzed twice, with a higher split to quantify cholesterol and with a lower split to measure all other sterols. The samples were analyzed on an Agilent 5977N mass-selective detector connected to an Agilent 7890B gas chromatograph equipped with a capillary HP5-MS column (30 m × 0.25 mm; 0.25 μm coating thickness; J&W Scientific, Agilent). Helium was used as a carrier gas (1 ml min^{-1}). The inlet temperature was set to 280°C, and the temperature gradient applied was 180°C for 1 min, 180–320°C at 5 K min^{-1} and 320°C for 5 min. Electron energy of 70 eV, an ion source temperature of 230°C and a transfer line temperature of 280°C were used. Spectra were recorded in the range of 70–600 Da/e (ChemStation Software D.01.02.16). Sterols were identified by the use of external standards.

Generation of BV2 *FDFT1* and *TREM2* knockouts

In order to generate the *FDFT1 KO* in BV2 cells, we used Cas9-gRNA Ribonuclease complexes to generate a cut in the genome 5' and 3' of *Fdft1* Exon 3. We used the online tool CRISPOR (https://doi.org/10.1093/nar/gky354) to select suitable Guide RNAs, with following settings. Genome: ''mus musculus UCSC Jun 2020 GRCm39/mm39''; Protospacer Adjacent Motif (PAM): '20bp-NGG – Cas9 S. Pyogenes'. The Guide RNAs used to generate the Knock Out were ATGGCGTGCCTGTAAAAAGA (including 5' addition of G) and GAGGACTTCCCCACGGTACT for the 5' and 3' cut, respectively. The RNP complexes for each guide RNA were generated individually at a ratio of 52 pmol:60 pmol (Cas9:gRNA) and co-nucleofected into BV2 cells using the P3 Primary Cell 4D-Nucleofector™ X Kit S. After 3 days, single cell clones were picked to ensure clonality of the generated population. Knockout of Exon 3 was confirmed via PCR using *Fdft1*Exon3KO-genotyping primers flanking the cut sites. Sanger Sequencing of the genotyping PCR product, and qPCR after serum starvation. All Guides were synthesized by Synthego and purchased as CRISPRevolution sgRNA EZ Kit. To generate the *TREM 2 KO* in BV2 cells we used the pSpCas9(BB)-2A-GFP plasmid (PX458; kindly provided by Feng Zhang targeting Exon 2 with the gRNA CATGGCCGGCCAGTCCTTG. 24 hours after nucleofection GFP-positive cells were isolated by FACS. Single-cell clones from the GFP-positive fraction were obtained by serial dilution and screened for genetic modifications in *Trem2* via PCR amplification of exons 2 and missense detection using T7 endonuclease I (NEB). Media and lysates of edited clones were analyzed by Western blot for TREM2 expression.

Generation of iPSC derived microglia cells

All stem cell work was performed following all relevant guidelines and regulations. Female human episomal iPSC line A18944 was obtained from ThermoFisher (#A18945). Human iPSC-derived hematopoietic progenitors were generated by using Stem Cell Technologies STEMdiff™ Hematopoietic Kit (# 05310) according to the manufacturer's directions. Briefly, iPSCs were split once they were 70–90% confluent after 5 min incubation in PBS/ EDTA in 1:100 ration into GelTrex coated 6-well plates to get around ~20 small colonies per well. Cells were left to recover overnight, and on the next day, the culture medium was changed to STEMdiff basal media containing supplement A. On day 2 days half of the medium was replaced with a fresh one. The next day (day 3) the medium was switched with STEMdiff basal media containing supplement B. Every other day (days 5, 7, 10) half of the medium was replaced with a fresh one. Cells were harvested on day 12 by collecting cell suspension, filtering through a 70 μm cell strainer, and titrating with DMEM/F12 and differentiated into microglia cells as described in Abud et al.[73] Cells were plated onto GelTrexcoated 6-well plates with 2 ml of iMGL-DM1 media with a cell density of 160.000-200.000 cells per well. iMGL-DM1 media contained the following growth factors: 25 ng/ml M-CSF (Peprotech, #300-25), 100 ng/ml IL34 (Peprotech, #200-34), and 50 ng/ml TGF-b (Peprotech,

#AF-100-21C). Cells were fed with 1 ml of medium every other day. Cells were split every 6-8 days if they were too confluent. iPSC were maintained on VTN-coated 6-well cell culture plates in a humidified incubator (5% CO2, 37°C). Experiments were conducted after 16 days of microglia differentiation.

Aggregation assay in cell culture

Aggregation assays were performed in BV2 macrophage mouse cell line and primary mouse glial cells. BV2 *Trem2* knockout cells were kindly provided by Michael Willem. Wildtype BV2 cells and *Trem2* knockout cells and *FDFT1 KO* cells were plated (1 x 10^4). Primary mouse microglia was established from 2-15 days old mice. Briefly, brains were digested using the neuronal tissue dissociation protocol (Miltenyi biotec), and cell solution was strained using a 40 μm strainer to get a single cell solution. Cell solution was then incubated with CD11b microbeads followed by incubation, and microglia was positively selected using LS columns and plated (4 x 10^4) on a PLL coated coverslips for imaging. Isolated primary microglia were cultivated in DMEM containing 1% penicillin-streptomycin, 1mM sodium pyruvate and 10 ng/ml M-CSF until confluent. For preparation of primary astrocytes, cell solution was incubated with ACSA-2 microbeads, plated (4 x 10^5) on a PLL coated coverslips and cultivated in DMEM containing 1% penicillin-streptomycin and 20% fetal bovine serum. Preparation of mixed glial cell culture was performed as previously described.[74] Briefly, cerebral cortices from P2 pups were dissected, minced, and digested. Dissociated cells were plated in poly-D-lysine-coated 75 cm^2 flasks, and maintained in DMEM containing 20% fetal bovine serum and 1% penicillin-streptomycin. After the cells became confluent (~10 days), cells were trypsinized and plated (4 x 10^5) on a PLL coated coverslips and cultivated until use.

If not stated differently, the following four aggregation treatment groups were prepared and incubated for 3 days until analysis. Namely, cells were treated either with a single dose of $A\beta_{42}$ (Anaspec, AS-64129-1; 1 μg/ml), a single dose of recombinant mouse APOE (N-terminally His-tagged, BiologicsCorp, 100 ng/ml), or a double treatment containing $A\beta_{42}$ and APOE while control untreated cells were cultured in parallel. HFIP monomeric $A\beta_{42}$ peptide was incubated in 1xPBS pH 7.4 at 37°C for 48 hours and directly applied to cell culture experiments. After 72 h of incubation, cells were washed and fixed with 4% paraformaldehyde and stored until staining. To test if purified APOE aggregates from *5xFAD* mice and human AD brain affects aggregation in BV2 cells, purified materials (100 ng/ml) were supplemented in addition to the above-mentioned standard treatments. Lysosomal inhibitors, Lys05 (1 μM), Bafilomycin (7,5 nM), and Leupeptin (5 μM), were added 1 h after the treatment of $A\beta_{42}$ and APOE, and cells were collected after 72 h. For induction of microglial activation, BV2 cells and primary microglia were treated with LPS (10 ng/ml), IFNγ (1 ng/ml) and Baricitinib (1 μM; InvivoChem,V0338) 2-24 h before $A\beta_{42}$ and APOE treatment. For comparing the effect of unlipidated and lipidated APOE, recombinant mouse APOE and POPC/cholesterol-lipidated mouse APOE (2.9 nM each) were used in single treatment or in combination with Aβ42. Cells were incubated for 72 h for the assessment of $MX04^+$ aggregates, and for 4 h for the assessment of intracellular Aβ-488/APOE uptake. For analysis of Aβ and APOE concentration-dependency against aggregate formation, consistent concentrations of APOE (100 ng/ml) or Aβ (2.5 μg/ml) were applied in combination with varying concentrations of the other protein (Aβ: 0-2.5 μg/ml, APOE: 0-100 ng/ml). For analysis using physiological APOE from human CSF, 100 ng/ml of purified APOE was incubated with primary microglia for 72 h in combination with 2.5 μg/ml of Aβ, and the same concentration of recombinant APOE4 + Aβ were used as a unlipidated control.

Preparation of amyloid protein extracts in mouse brains by DEA/RIPA/FA

For Western blotting of amyloid proteins, mouse brains were perfused with PBS, dissected into cortices and other regions, snap-frozen, and stored at −80°C until use. After pulverization of cortices by a liquid nitrogen cooled mini mortar (Sigma), 20-25 mg of brain powder were transferred to soft tissue homogenizing Precellys tubes (Bertin Technologies). 130-150 μl of ice-cold DEA buffer (0.2% diethylamine in 50 mM NaCl, pH 10, and protease inhibitor mix (Life)) was added to generate soluble extracts. The powder was homogenized at 6,500 rpm. for 30 s at 4°C using a sample homogenizer (Bertin Technologies). The pellet from 10 min centrifuge at 4,000 g (4°C) was resuspended in 130-150 μl RIPA buffer (20 mM Tris/HCl pH 7.5, 150 mM NaCl, 2.5 mM EDTA, 1% NP-40, 1% sodium deoxycholate, 2.5 mM sodium pyrophosphate, and protease inhibitor mix (Life)) by 30 min shaking at 4°C, while the supernatant was ultracentrifuged (30 min, 55,000 rpm, 4°C). The supernatant from the ultracentrifugation was collected as DEA fraction, and the pH was adjusted by adding 10% 0.5 M Tris/HCl pH 6.8. The RIPA lysates in the Precellys tubes were centrifuged at 4,000 g (10 min at 4°C). The remaining pellet was homogenized in 60-70 μl of 70% formic acid (FA) (Merk) while the supernatant was combined with the pellet from the first ultracentrifugation after solubilizing with 50 μl of fresh RIPA buffer. The combined RIPA lysates were subjected to ultracentrifugation (60 min, 55,000 rpm, 4°C), and the supernatant was collected as RIPA fraction. The FA lysate was sonicated for 7 min in a bath-sonicator (Sonorex RK100H, Bandelin), centrifuged at 20,000 g (30 min at 4°C). The supernatant (20 μl) was neutralized with 380 μl 1 M Tris–HCl buffer at pH 9.5, and used as FA fraction. Total protein concentrations in DEA and RIPA fractions were determined using the BCA assay (Interchim) and adjusted by each buffer before further analysis. Concentrations of FA fractions were adjusted based on those of RIPA fractions.

Western Blot

For SDS-PAGE analysis, proteins were mixed with 4x Laemmli Sample Buffer (Bio Rad) containing 2-mercaptoethanol and boiled for 5 min at 95°C. After separating the proteins on Tris-Tricine gels (10–20%, Thermo Fisher Scientific) with the XCell SureLock Mini-Cell system (Novex), proteins were transferred to nitrocellulose membranes (Amersham™ Protran® Western blotting membranes, 0.2 μm, Merk) and boiled for 5 min in PBS. The membranes were then incubated with a blocking solution containing 0.2% I-Block (Thermo Fisher Scientific) and 0.1% Tween 20 (Sigma) in PBS for 1 h, followed by overnight incubation with primary antibodies in

Please cite this article in press as: Kaji et al., Apolipoprotein E aggregation in microglia initiates Alzheimer's disease pathology by seeding β-amyloidosis, Immunity (2024), https://doi.org/10.1016/j.immuni.2024.09.014

the blocking solution. The rat monoclonal 2D8 antibody against Aβ was described before.[75] Hybridoma-derived 2D8 antibody was kindly provided by Michael Willem. Other primary antibodies include anti-amyloid precursor protein [Y188] (abcam), anti-β-actin (Sigma), anti-APOE (mouse) (Thermo Fisher Scientific), anti-APOE (human) (Millipore), anti-Halo (Promega), anti-tau [Tau-5] (Thermo Fisher Scientific), anti-p-tau (Thermo Fisher Scientific), anti-ferritin heavy chain (abcam) antibodies. After removal of the antibody, membranes were washed three times in TBS-T (0.2% Tween 20, Sigma) buffer, subsequently incubated with secondary HRP antibodies (Thermo Fisher Scientific) for 1 h at room temperature, and washed three times again with TBS-T. To perform ECL detection, horseradish peroxidase substrate (ECL, GE Healthcare or ECL Plus, Thermo Scientific) was added to the membranes, and the resulting signals were captured on X-ray films (Super RX Medical X-Ray, Fujifilm). These films were then developed using an automated film developer (CAWOMAT 2000 IR, CAWO). For Native PAGE analysis, proteins were mixed with Novex™ Tris-Glycine Native Sample Buffer (2X) (Invitrogen) and loaded onto Tris-Glycine gels (4-12%, Thermo Fisher Scientific) with the XCell SureLock Mini-Cell system (Novex). Proteins were transferred to pre-activated PVDF membranes (Invitrolon™ PVDF / Filter Paper Sandwiches, 0.45 μm, Invitrogen) and boiled for 5 min in PBS before the incubation with the blocking solution. Antibodies used were listed in key resources table.

Isolation of sarkosyl-insoluble fractions and PBS extracted lysate

Sarkosyl-insoluble fractions from mouse brains were extracted as previously described with some modifications[36,76] and used for Western Blot and stereotactic injection. Briefly, 20-40 mg of pulverized mouse cortices in Precellys tubes (Bertin Technologies) was homogenized in 10 vol (w/v) A68 extraction buffer (10 mM Tris-HCl, pH 7.5, 0.8 M NaCl, 10% sucrose and 1 mM EGTA) using a sample homogenizer (6,500 rpm. for 30 s at 4°C, Bertin Technologies). Homogenates were brought to 2% sarkosyl and incubated for 30 min at 37° C. Following a 10 min centrifugation at 10,000 g, the supernatants were spun at 113,000 g for 20 min at 25 °C. The pellets were washed with saline and ultracentrifuged as before. The resulting pellets were resuspended in 30 μl PBS for stereotaxic injection or in 30-50 μl 30 mM Tris-HCl (pH 7.4) for Western Blot. After 15 s sonication, the solutions were centrifuged at 1,000 g for 5 min at 4 °C, and the supernatant was collected as sarkosyl-insoluble fractions. For stereotactic injections, Aβ in sarkosyl-insoluble fractions from 12-month-old *5xFAD* and 12-month-old *5xFAD ApoE KO* mice were quantified by Western Blot, and adjusted to the same concentration. Synthetic beta-amyloid peptide (1-42) (abcam) was used as the standards for the quantification. Preparation of PBS extracted lysate was conducted as previously described.[77] Briefly, 30 mg of pulverized mouse cortex, derived from 12-month-old *5xFAD* mice, was homogenized in 10 vol (w/v) sterile PBS using a sample homogenizer (6,500 rpm. for 30 s at 4°C, Bertin Technologies) and sonicated for 15 s (30% amplitude, Digital Sonifier W-250D, Branson). The crude brain homogenate was centrifuged for 5 min (at 3,000 g, 4°C), and the supernatant was stored at −80°C until use.

APOE aggregate isolation from *ApoE-Halo 5xFAD* mouse and human brain

For mouse APOE aggregate isolation, the isolation of sarkosyl-insoluble fraction was conducted as described above. In order to increase the aggregate concentration, cortices from 2-4 *ApoE-Halo 5xFAD* mice (5-6-month-old) were pooled and homogenized in 5 vol (w/v) extraction buffer (10 mM Tris-HCl, pH 7.5, 0.8 M NaCl, 10% sucrose and 1 mM EGTA) using a sample homogenizer (6,500 rpm. for 30 s at 4 °C, Bertin Technologies). The pellets from ultracentrifuge after saline wash were resuspended in 200 μl 30 mM Tris-HCl (pH 7.4), sonicated by bath-sonicator (Sonorex RK100H, Bandelin) for 3 min, and centrifuged at 1,000 g for 5 min at 4 °C. Purification of APOE aggregates from the sarkosyl-insoluble fraction was conducted by immunoprecipitation using Halo-Trap Magnetic Agarose (Chromotek) according to manufacturer's instruction. After 2:3 dilution with a dilution buffer (10 mM Tris/Cl pH 7.5, 150 mM NaCl, 0.5 mM EDTA), sarkosyl-insoluble fractions were loaded onto the agarose beads and incubated overnight at 4 °C with continuous mixing. Beads elution was carried out by adding 200 mM glycine pH 2.5 to the beads and followed by the addition of 10% volume of neutralizing buffer (1M Tris, pH 10.4). The solution was then dialyzed against PBS by using Slide-A-Lyzer™ Dialysis Cassettes (Thermo Fisher Scientific, 10kDa). The dialyzed solution was collected, snap-frozen and stored at −80°C as mouse APOE aggregates. For preparation of mouse ApoE-depleted Sarkosyl-insoluble fraction, which was used for stereotaxic injections, the beads-unbound flow-through from above-mentioned Halo-trap immunoprecipitation was used after normalizing the protein concentration by NanoOrange™ Protein Quantitation Kit (Thermo Fisher Scientific). For human APOE aggregate isolation, 200 mg of temporal cortex from Alzheimer's disease patient brain was homogenized in 20 vol (w/v) extraction buffer (10 mM Tris-HCl, pH 7.5, 0.8 M NaCl, 10% sucrose and 1 mM EGTA) using a sample homogenizer (6,500 rpm. for 30 s at 4 °C, Bertin Technologies). After addition of sarkosyl (2% as the final concentration), lysates were incubated for 24h at 37 °C with shaking. The lysates were then centrifuged at 10,000g for 10 min, and the supernatant was further ultracentrifuged 113,000 g for 20 min at 25 °C. After washing the pellet with saline, the pellet was solubilized in 30 mM Tris-HCl by pipetting and sonication for 3 min by bath-sonicator. The debris were removed by centrifuge at 1000 g for 5 min. The sarkosyl-insoluble fractions were incubated overnight with 1:25 volume of biotinylated APOE antibody (0.81 mg/ml, Novus Biologicals) at 4 °C with agitation at 400 rpm. Immunoprecipitation by streptavidin-conjugated magnetic beads, Dynabeads™ M-280 Streptavidin (Thermo Fisher Scientific), was performed according to the manufacturer's instructions. For Aβ immuno-depletion, the elute was mixed with 1:75 volume of biotinylated anti-β amyloid, 1-16 antibody (BioLegend) and incubated overnight at 4 °C with agitation at 400 rpm. After removal of antibody-bound Aβ by Dynabeads™ M-280 Streptavidin (Thermo Fisher Scientific), the flow-though was again added with 1:75 volume of biotinylated anti-β amyloid, 1-16 antibody, and incubated at 4 °C for 6h with agitation. The flow-through from the second immuno-depletion was then dialyzed overnight against PBS by using Slide-A-Lyzer™ Dialysis Cassettes (Thermo Fisher Scientific, 10kDa). The solution after dialysis was centrifuged at 1,000 g for 10 min at 4°C, and the supernatant was stored at −80°C as human APOE aggregates. For

both mouse and human APOE aggregates, the enrichment of APOE and absence of Aβ were analyzed by Western Blot while the aggregation status was confirmed by Native-PAGE and EM. Antibodies used were listed in key resources table.

Isolation of brain-derived RIPA-soluble APOE-Halo from *ApoE-Halo* mouse

Purification of RIPA-soluble APOE-Halo from *ApoE-Halo* mice was enabled through immuno-precipitation of Halo-tagged proteins using Halo-Trap Magnetic Agarose (Chromotek). Three 4-month-old *ApoE-Halo* mice were perfused with PBS, and the brainstems were transferred to Precellys tubes (Bertin Technologies). The brains were homogenized in 2 vol (w/v) RIPA buffer (20 mM Tris/HCl pH 7.5, 150 mM NaCl, 2.5 mM EDTA, 1% NP-40, 1% sodium deoxycholate, 2.5 mM sodium pyrophosphate, 1mM PMSF, and protease inhibitor mix (Life)) using a sample homogenizer (6,500 rpm. for 30 s at 4°C, Bertin Technologies). The lysates were then centrifuged at 17,000g for 20 min at 4°C, and the supernatant was diluted 2:3 with a dilution buffer (10 mM Tris/Cl pH 7.5, 150 mM NaCl, 0.5 mM EDTA) containing 1mM PMSF and protease inhibitor mix (Life). The diluted lysates were incubated overnight with the agarose beads at 4°C with continuous mixing. Beads elution was performed with 200 mM glycine pH 2.5, and the elute was dialyzed overnight against PBS by using Slide-A-Lyzer™ Dialysis Cassettes (Thermo Fisher Scientific, 10kDa). After centrifuge at 1,000g for 10 min (4°C), supernatant was collected as brain-derived RIPA-soluble APOE-Halo and stored at −80°C until use.

Preparation of BV2 cell lysate for stereotactic injection

BV2 cells in 15 cm culture dishes were harvested 3 days after incubation either with Aβ alone or with Aβ plus APOE. After three times wash with PBS, the cell pellets from the centrifuge at 5000 rpm (5 min at 4°C) were subject to one cycle of freeze-thaw and resuspended in 100 μl PBS. Subsequently the lysates were sonicated for 15 s with a probe-sonicator (30% amplitude, Digital Sonifier W-250D, Branson) and centrifuged at 3,000 g for 5 min at 4°C. The total protein concentrations of the supernatant were normalized to 40 mg / ml using Pierce™ BCA Protein Assay Kit (Thermo Fisher Scientific). The lysates were snap-frozen and stored at −80°C until use.

Stereotactic injection of sarkosyl-insoluble fractions, PBS-extracted lysate, APOE aggregates (mouse and human) and BV2 cells lysates

Animals were anesthetized with MMF (medetomidine 0.5 mg/kg, midazolam 5.0 mg/kg fentanyl 0.05 mg/kg). The mice were placed in a stereotactic frame and, after incision of the skin, small holes were drilled in the skull at the appropriate locations. The following coordinates were used to target prefrontal cortices unilaterally or bilaterally: AP + 2 mm, ML ± 0.55 mm, DV 1.8 mm (relative to Bregma). Each injection was performed with the speed of 150 nl/min, and the needle was left in situ for 5 mins before being slowly withdrawn. The injection volume per hemisphere was 1.5 μl for all the injection materials except TMR-Cholesterol (1.0 μl, 10 ng of TMR-Cholesterol in 10% DMSO in PBS). After surgery, the skin was closed with silk sutures, and the animal was put on a warm pad to prevent hypothermia.

Immunohistochemistry and immunocytochemistry

Mice were anesthetized using ketamine/xylazine, perfused with PBS and the extracted tissue was postfixed with 4% paraformaldehyde (PFA) for 4-6 h, cryoprotected in 30% sucrose for 3 nights and subsequently embedded in Tissue-Tek OCT cryo embedding matrix followed by freezing the tissue on dry ice. Brain samples were cut in 16 μm sections (CryoStar NX70 HOMVP) and stored at -80°C. Sections of *APP/PS1* and *APP/PS1-Trem2-KO* mice were kindly provided by Christian Haass. Immunohistological staining was done on sections that were adjusted to RT for 30 min and washed with PBS to remove the excess embedding matrix. For all immunofluorescent staining except Aβ labeling, sections were transferred in citrate buffer (0.01 M, pH 6.0) for antigen retrieval. Tissue permeabilization was performed by incubating sections with 0.5% Triton X100 for 10 min. For immunofluorescence detection, blocking was performed using a mixed blocking solution (2.5% bovine serum albumin, 2.5% fish gelatin, 2.5% fetal calf serum in PBS). For staining procedures requiring mouse antibodies, sections were additionally blocked with 1:100 mouse Fab fragment blocking (715-007-003, Jackson ImmunoResearch) in PBS for 1 h. Primary antibodies were anti-Aβ 1-11 (Biolegend), anti-Aβ 2D8 (provided by Michael Willem), anti-Aβ 6E10 (Biolegend), anti-Aβ D3E10 (Cell signaling), anti-Aldh1l1 (Sigma), anti-BCAS1(Novus Biologicals), anti-CD68 (Bio-Rad), anti-GFAP (Synaptic Systems), anti-IBA1 (Synaptic Systems), anti-NeuN (Millipore), anti-LAMP1 (Santa Cruz), anti-PDFGRα (R&D systems), anti-STAT1 (CST) diluted in antibody diluent (0.625% bovine serum albumin, 0.625% fish gelatin, 0.625% fetal calf serum in PBS) and incubated for 24-72 h followed by incubation with fluorophore-coupled secondary antibodies Alexa488 Donkey α-chicken (Jackson), Alexa488 Donkey α-guinea pig (Sigma), Alexa488 Donkey α-rat (Invitrogen), Alexa555 Donkey α-rat (Thermo), Alexa647 Goat α-mouse (Thermo), Alexa647 Donkey α-rabbit (Thermo), Alexa647 Donkey α-rat (Jackson), for 1 h at RT. APOE-Halo was detected by TMR Halo ligand (Promega), and ligand staining was implemented in the secondary antibody staining step. To visualize β-sheet structure, either MXO4, ThiazineRed, or Thioflavine S was used. For MXO4 (Tocris) staining, tissue was incubated with 4 μg/ml MXO4 in 50% ethanol for 30 min and washed for 5 min with 50% ethanol followed by three times wash with PBS. Thiazine Red (Sigma) was used in 1:1000 dilution in PBS for 15 min and washed three times with PBS. Thioflavine S (Sigma) was stained by using 1% Thioflavine S filtered solution and incubated for 8 min. Excess dye was removed by 2 x 3 min wash with 80% ethanol, 1 x 3 min wash with 95% ethanol, and 3 x 3 min wash with distilled water. After β-sheet structure staining, nuclear labeling was performed using either Hoechst (Thermo Fisher) or NucRed (Invitrogen). For human staining, blocking of endogenous peroxidase activity with 3% hydrogen peroxide was performed, which was followed by antigen retrieval with citrate buffer (0.01 M, pH 6.0) and blocking with above-mentioned mixed blocking solution. Incubation of three different primary antibodies and corresponding

secondary antibodies was performed individually in different steps. Namely, incubation with first primary antibody anti-APOE 8D4 (provided by Michael Willem) for 24 h was followed by HRP-coupled secondary antibody (Goat α-rabbit, Thermo) incubation for 1 h at RT and subsequent binding with Opal dye 570 (Perkin Elmer). Repetitive boiling step with citrate buffer as described was performed before incubating with the next primary antibody anti-Aβ1-11 (Biolegend) for 24 h, which was then followed by HRP-coupled secondary antibody (Thermo) incubation for 1 h at RT and subsequent binding with Opal dye 620 (Perkin Elmer). Subsequent to the last boiling step with citrate buffer as described, the third primary antibody incubation anti-IBA1 (Synaptic Systems) for 24 h was followed by HRP-coupled secondary antibody (Invitrogen) incubation for 1 h at RT and subsequent binding with Opal dye 520 (Perkin Elmer) Serial antibody staining was followed by MXO4 staining and nuclear labeling as described previously. For immunocytochemistry, cells were stained after 1 min permeabilization with 0.1% Triton and 1 h blocking with previously described blocking solution. Primary antibody incubation was performed overnight and secondary antibody incubation for 1 h at RT. After removal of secondary antibody, cells were subject to MXO4 and nuclear labeling as described earlier.

Image acquisition and quantification

Optical sections were acquired with a confocal laser-scanning microscope (Zeiss LSM 900 AiryScan) using a LD C-Apochromat 40x/1.1 Water objective (Zoom factor 0.5 -1.3) or objective Plan-Apochromat 63x/1.4 Oil DIC M27 (Zoom factor 1.3-2.5). Z-step was kept between 0.8 to 1.5 μm for quantitative imaging and 0.22 μm for 3D reconstruction imaging. Images were acquired in bidirectional mode (Aryscan Mode SR:4.1 2D Auto) and LSM scan speed was kept between 5 to 7. For the 3D reconstructions, 3D images were first generated from the individual z-planes in the Surpass view option of Imaris x64 (version 9.2.0, Bitplane). The region of interest was then segmented and a "Surface" was created for each channel, using the Surface creator tool. For immunohistochemistry analysis two to three sections from each animal were analyzed using Image J software.[70] For analysis of plaque morphology, MX04 intensity (IntDen) measurement was performed. MXO4 intensities in relation to total plaque area, mean plaque area and mean plaque intensity were analyzed. Plaque size was determined using an automated threshold strategy (FIJI Software). For injection experiments, tile scan images at the injection site identified by IBA1 reactivity were analyzed by fixed threshold method and particle analyzer (Size 0.2 μm^2 -infinity, circularity 0-1) to determine $MX04^+$ plaque number in acquired z-stacks. Quantification of MX04+ extracellular plaques and intracellular MX04+ aggregates were performed on single z-planes using cell counter plug in. Mean size of 25-30 microglial (IBA1+) intralysosomal (CD68+) MX04+ aggregates per mouse in *APP/PS1* and *APP/PS1 Trem2 KO* mice were quantified by fixed threshold method on consecutive single z-planes. MX04+ aggreges in cell culture experiments were quantified by fixed threshold method and particle analyzer (Size 0.01 μm^2 -infinity, circularity 0-1).

Light sheet microscopy

After perfusion with 4% PFA, immersion fixed brain hemispheres were processed for whole mount tissue Congo red labelling and subsequent clearing following a modified iDISCO protocol.[78] Light sheet microscopy was performed using a LaVision Ultramicroscope II equipped with 2x objective, corrected dipping cap and zoom body. Hemispheres were mounted onto the sample holder with the medial side down and placed into the imaging chamber filled with Eci to acquire sagittal imaging planes. Images were acquired in the mosaic acquisition mode with the following settings: 5 μm light sheet thickness, 20% sheet width, 0.154 sheet numerical aperture, 4 μm z-step size, 1000 x 1600 px field of view, 4 x 4 tiling, dual light sheet illumination, and 100 ms camera exposure time. Red fluorescence was recorded with 561 nm laser excitation at 80% laser power and a 585/40 nm emission filter. Autofluorescence was recorded with 488 nm laser excitation at 50% and 525/20 nm emission filter. Images were imported into Vision4D v3.2 (Arivis) and stitched usingthe tile sorter setup. Partly, images were imported and stitched using Imaris Importer and Stitcher v9.1 (Bitplane). Rendered hemibrains were then processed and two main regions of interest were manually annotated based on the sagittal Allen mouse brain atlas, namely isocortex and hippocampus. All ROIs were first traced manually in 2D planes to automatically extrapolate the 3D ROIs. Next, we segmented amyloid plaques within the ROIs. Plaques were segmented using the blob finder algorithm in Vision4D with the following parameters: 20 μm object size, 10-15% probability threshold, and 0% split sensitivity. Once segmentation has been performed, a stringent noise removal was performed by deleting objects with voxel sizes < 10 from the object table. Additional noise due to blood vessels were removed manually.

Preparation of monomeric/tetrameric recombinant APOE4

Isolation of monomeric / tetrameric APOE was performed as described.[38] Briefly, N-terminally His-tagged recombinant APOE4, which was bacterially overexpressed and purified by Ni-IDA (> 90% purity and endotoxin < 0.1 EU/μg), was produced by BiologicsCorp. Lyophilized protein was reconstituted in a 4 M guanidine hydrochloride on ice and injected onto a Superdex^{TM} 200 Increase 10/300GL column equilibrated in TBS (10 mM Tris, 150 mM NaCl, 0.25 mM EDTA, pH 7.4) for FPLC. The protein eluted as two peaks and proteins in each peak fraction were analyzed by Native-PAGE to confirm that the first and second peaks represented aggregated and monomeric / tetrameric APOE, respectively. Here, monomeric / tetrameric APOE was collected and snap-frozen in liquid nitrogen and stored at –80 °C until analysis. FPLC of monomeric / tetrameric APOE after a cycle of freeze / thaw showed no change in aggregation state when compared with the freshly prepared protein. Concentration of FPLC-purified monomeric / tetrameric APOE4 was determined by absorbance measurements at 280 nm using an extinction coefficient of 44,460 $M^{-1} \cdot cm^{-1}$.

Preparation of POPC/cholesterol-lipidated APOE

Lipidation of recombinant mouse and human APOE was performed as previously described.[79] The mixture of Palmitoyl-2-oleoyl-sn-glycero-3-phosphocholine (POPC, Avanti Lipids) and unesterified cholesterol (Sigma) in a 90:5 molar ratio was comixed in chloroform and dried using a continuous flow of nitrogen gas in a glass vial. For the preparation of TMR-lipidated APOE-Halo, APOE3, and APOE4, the same molar concentration of TopFluor® TMR Cholesterol (Avanti) was used instead of untagged cholesterol. The resulting lipids were then suspended in sterile PBS to obtain a concentration of 5 mg lipids/ml PBS (5.11 mg lipids/ml PBS for TMR-lipidated APOE-Halo). The solution was vortexed thoroughly for 3 min and kept at RT for 30min. For POPC/TMR-cholesterol liposomes, solutions were solubilized further by pipetting and 2-3 min sonication using bath-sonicator (Sonorex RK100H, Bandelin). Subsequently, sodium cholate (50 mg/ml, Sigma) was slowly titrated into the liposome solution (3 volumes of sodium cholate for 1 volume of lipids). After 5 min of gentle vortex, the solution was kept at RT for 30–60 min. Recombinant mouse APOE, human APOE3, human APOE4, or mouse APOE-Halo (BiologicsCorp) was then added to the liposome solution (APOE : POPC : cholesterol, molar ratio of 1 : 90 : 5) and mixed gently for 5 min by tapping. The solution was kept at room temperature for 1 h and dialyzed for 3 days against PBS at 4°C using Slide-A-Lyzer™ Dialysis Cassettes (Thermo Fisher Scientific, 10kDa). Lipidated APOE particles were analyzed by Native-PAGE, DLS, EM, and density gradient ultracentrifugation with Optiprep™ Density Gradient Medium (Sigma). APOE concentrations were determined by immunoblot, and samples were stored in –80°C until use.

Analysis of intracellular APOE-Halo lipidation status by density ultracentrifugation

Primary microglia was treated with 0.2 μM POPC/Cholesterol-lipidated mouse APOE-Halo for 1h or 4h following overnight preincubation with serum-free medium. After washing the cells twice with PBS, cells were scraped and collected in 160 μl PBS without using detergent. Cells were then lysed through 3 cycles of freeze and thaw and centrifuged at 10.000g for 10 min at 4°C. The supernatant was collected as the cell extracts and subject to density ultracentrifugation by OptiPrep™ Density Gradient Medium (Sigma). In order to exclude the possibility of potential delipidation due to the lysis step, culture medium containing POPC/Cholesterol-lipidated mouse APOE-Halo was processed equally to cell extracts with the same cycles of freeze/thaw and the centrifuge. Density ultracentrifugation was performed as previously described with a mild modification.[80] Either cell extracts or medium were mixed with 60 % Optiprep in 2:3 ratio to reach 36% Optiprep concentration and transferred to an ultracentrifuge tube (Beckman Coulter) (Figure S7E). 24% and 0% Optiprep solutions diluted with 10mM HEPES (500 μl each) were layered on top, and ultracentrifugation was performed at 5,4000 rpm for 3 hours at 4°C. The POPC/cholesterol-lipidated APOE-Halo floated to the region between the 0% and 24% Optiprep. Practically, the top 500 μl was discarded as 0% Optiprep fraction, and the next 150 μl was collected as the floating fraction. After removing the residual 24% Optiprep solution (350 μl), the solution remaining in the bottom was collected as the non-floating fraction. Both floating and non-floating fractions were analyzed by SDS-PAGE.

POPC/TMR-lipidated APOE uptake analysis

TMR-cholesterol lipidated APOE-Halo (100 ng/ml) and TMR-cholesterol lipidated APOE3 and APOE4 (2.5 μg/ml) were treated to primary microglia and incubated for each designated time. TMR-cholesterol+ area in PLIN2+ lipid droplets were quantified.

Physiological APOE purification from human CSF

Pooled CSF of healthy individuals were incubated overnight with 1:25 volume of biotinylated APOE antibody (0.81 mg/ml, Novus Biologicals) at 4 °C with agitation at 400 rpm. Immunoprecipitation by streptavidin-conjugated magnetic beads, Dynabeads™ M-280 Streptavidin (Thermo Fisher Scientific), was performed according to the manufacturer's instructions. Pre-incubated CSF was incubated with beads for 30 min at RT, and flow-through was discarded. After 3 cycles of wash by PBS, beads elution was carried out by adding 200 mM glycine pH 2.5 to the beads and followed by the addition of 10% volume of neutralizing buffer (1M Tris, pH 10.4). APOE concentration was measured by immunoblot using recombinant APOE4 as standards.

APOE real-time quaking-induced conversion (RT-QuIC) assay and preparation of recombinant APOE4 aggregates

Purified monomeric / tetrameric APOE4 was incubated with / without APOE aggregates from a human AD brain continuously for 12.5-18 days in the presence of 10 μM Thioflavin T (ThT). Monomeric / tetrameric APOE4 was prepared in two different conditions; 1) high concentration (500 μg/ml) and low volume (100 μl/sample), and 2) low concentration (220 μg/ml) and high volume (240 μl/sample). For comparison between unlipidated/lipidated APOE3 and APOE4, 14.2 μM (500 μg/ml) of purified monomeric/tetrameric APOE or the same molar concentration of POPC/cholesterol-lipidated APOE was incubated for 18-21 days with 10 μM ThT. All samples were added with 10% volume of 10 x PBS before the start of incubation. Black 96-well plates with a clear bottom (Corning) were sealed and incubated in FLUOstar Omega (BMG Labtech) plate reader at 37°C with intermittent double orbital shaking at 400 rpm for 1 min, followed by 1 min rest. ThT fluorescence was measured using 448 nm excitation and 482 nm emission filter, and the values from every 4 h were plotted. For preparation of recombinant APOE4 aggregates for TEM observation, stereotaxic injections, and $A\beta_{42}$ RT-QuIC assay, above-mentioned monomeric / tetrameric APOE4 was incubated for 12.5-18 days after addition of 10% volume of 10 x PBS in the absence of ThT.

Aβ RT-QuIC assay

Stocks of HFIP-treated monomeric $A\beta_{42}$ (Anaspec, AS-64129-1) were prepared at 1 mg/ml in DMSO and kept frozen until use. Shortly before analysis, stocks of $A\beta_{42}$ were diluted with PBS to 10 μM and aliquoted in black 96-well plates with a clear bottom (Corning)

Please cite this article in press as: Kaji et al., Apolipoprotein E aggregation in microglia initiates Alzheimer's disease pathology by seeding β-amyloidosis, Immunity (2024), https://doi.org/10.1016/j.immuni.2024.09.014

(100 μl/well). After addition of 5% volume of 200 μM Thioflavin T (10 μM as a final concentration), $A\beta_{42}$ in each well was mixed either with 1) 2μl of 0.5 mg/ml APOE3 incubated for 3 weeks in the presence of 10% volume of 10 x PBS, or 2) 2μl of 0.5 mg/ml APOE4 incubated for 3 weeks in the presence of 10% volume of 10 x PBS, or 3) equal volume of TBS as a control. Plates were sealed and incubated in FLUOstar Omega (BMG Labtech) plate reader at 37°C with intermittent double orbital shaking at 400 rpm for 5 min, followed by 5 min rest. ThT fluorescence was measured using 448 nm excitation and 482 nm emission filter, and the values from every 10 min were plotted.

Circular dichroism (CD) spectroscopy

For chronological analysis of incubated APOE4, monomeric / tetrameric protein (0.15 mg/ml) was prepared in TBS and incubated at 37°C for various times. Circular Dichroism spectra were measured with a Chirascan V100 instrument (Applied Photophysics, UK). A cuvette with 0.2 cm path length was filled with 160 μl of the APOE4 solution. Measurements were performed at 25°C, 190 – 260 nm, with 4 repeats. Control spectra obtained with TBS buffer alone were subtracted from the experimental spectra. The measured values (mdeg) at different time points were plotted. For comparison between unlipidated/lipidated APOE3 and APOE4, 14.2 μM (500 μg/ml) of purified monomeric/tetrameric APOE or the same molar concentration of POPC/cholesterol-lipidated APOE was incubated for 3 weeks. The mean residue ellipticity ([Θ] in deg cm^2 $dmol^{-1}$) was calculated as previously described.[37] Protein concentrations were measured by a NanoDrop spectrometer by measuring the absorbance at 280 nm using an extinction coefficient of 44,460 L mol^{-1} cm^{-1}.

Negative staining and transmission electron microscopy (TEM)

For transmission electron microscopic (TEM) observation, carbon coated copper grids (Science Services) were glow discharged for 30 sec in a Harrick plasma cleaner (PDC-32G-2) to facilitate adsorption. After fixing the grid by anti-capillary inverse tweezers (Dumont) a volume of 1.5 μl of the sample was deposited onto the grid for 2 min and blotted shortly using filter paper (Whatman). Negative staining was performed by addition of 1.5 μl 1% uranyl acetate in water for 30 s. After blotting, the grid was air dried for at least 30 min. Immunogold staining was performed on plasma-treated carbon coated nickel grids (Science Services). After adsorption of the APOE aggregates and washing, the samples were incubated in blocking buffer (5% acetylated BSA in distilled water). The primary antibodies (rabbit anti-Halo, 1:500, Promega, rabbit anti-APOE, 1:500, Thermo-Fisher) in blocking buffer were added for 90 min, washed three times in water and blotted. After secondary antibody (goat anti rabbit 10 nm gold, 1:20, Aurion) incubation for 90 min and three washing steps, the grid was contrasted in 1% uranyl acetate in water for 1 min the dark. The grids were blotted and air-dried for 30 min. Transmission Electron Microscopy micrographs were acquired on a JEM 1400plus (JEOL) equipped with a XF416 camera (TVIPS) and the EM-Menu software (TVIPS).

Volume scanning electron microscopy

For correlative EM, mice were anesthetized using ketamine/xylazine and perfused with PBS, the extracted tissue was postfixed in the fixative (4% PFA, 2.5% glutaraldehyde in 0.1 M cacodylate buffer) for 24 h and processed by cutting 40 μm vibratome sections. Section were postfixed with 2.5% glutaraldehyde in 0.1 M cacodylate buffer (Science Services) for EM analysis and subjected to a standard rOTO contrasting procedure.[81] After postfixation in 1% osmium tetroxide (Electron Microscope Services), 1.5% potassium ferricyanide (Sigma-Aldrich) in 0.1 M sodium cacodylate, staining was enhanced by reaction with 1% thiocarbohydrazide (Sigma-Aldrich) for 45 min at 40°C. The tissue was washed in water and incubated in 1% aqueous osmium tetroxide, washed and further contrasted by overnight incubation in 1% aqueous uranyl acetate at 4°C and 2 h at 50°C. Samples were dehydrated in an ascending ethanol series and infiltrated with LX112 (LADD). Tissue was serially sectioned at 100 nm thickness on to carbon nanotube (CNT) tape (Science Services) on an ATUMtome (Powertome, RMC) using a 35° ultra-diamond knife (Diatome). CNT tape stripes were assembled on to adhesive carbon tape (Science Services) attached to 4 inch silicon wafers (Siegert Wafer) and grounded by adhesive carbon tape strips (Science Services). EM micrographs were acquired on a Crossbeam Gemini 340 SEM (Zeiss) with a four-quadrant backscatter detector at 8 kV. Overview scans were taken at 200 nm lateral and higher resolution scans at 10 nm lateral resolution. Serial section data were aligned by a sequence of automatic and manual processing steps in Fiji TrakEM2 and relevant regions selected.

QUANTIFICATION AND STATISTICAL ANALYSIS

Data are shown as mean ± SEM. No statistical methods were used to predetermine sample sizes, but our sample sizes are similar to those generally employed in the field. Each dot represents one animal. Normal distribution of the samples was tested using the Shapiro–Wilk test. For statistical analysis, paired or unpaired Student's t-test, or if appropriate the Mann–Whitney U-test, was used to compare two groups. Two-sided, one-way analysis of variance (ANOVA) followed by post hoc Tukey's test was used for multiple comparisons. Tests were chosen according to their distribution. In all tests, a P value < 0.05 was considered significant with $^*P < 0.05$, $^{**}P < 0.01$ and $^{***}P < 0.001$. Statistical analyses were done using GraphPad Prism (GraphPad Software, Inc.). Data acquisition and analysis were performed in a blinded manner. No animals were excluded from the analyses.